01-04   January 2004

TECH BRIEFS

NATIONAL AERONAUTICS AND SPACE ADMINISTRATION

- **Technology Focus**

- **Computers/Electronics**

- **Software**

- **Materials**

- **Mechanics**

- **Machinery/Automation**

- **Manufacturing**

- **Bio-Medical**

- **Physical Sciences**

- **Information Sciences**

- **Books and Reports**

INTRODUCTION

Tech Briefs are short announcements of innovations originating from research and development activities of the National Aeronautics and Space Administration. They emphasize information considered likely to be transferable across industrial, regional, or disciplinary lines and are issued to encourage commercial application.

Availability of NASA Tech Briefs and TSPs

Requests for individual Tech Briefs or for Technical Support Packages (TSPs) announced herein should be addressed to

National Technology Transfer Center

Telephone No. **(800) 678-6882** or via World Wide Web at **www2.nttc.edu/leads/**

Please reference the control numbers appearing at the end of each Tech Brief. Information on NASA's Commercial Technology Team, its documents, and services is also available at the same facility or on the World Wide Web at **www.nctn.hq.nasa.gov**.

Commercial Technology Offices and Patent Counsels are located at NASA field centers to provide technology-transfer access to industrial users. Inquiries can be made by contacting NASA field centers and program offices listed below.

NASA Field Centers and Program Offices

Ames Research Center
Carolina Blake
(650) 604-1754
carolina.m.blake@nasa.gov

Dryden Flight Research Center
Jenny Baer-Riedhart
(661) 276-3689
jenny.baer-riedhart@dfrc.nasa.gov

Goddard Space Flight Center
Nona Cheeks
(301) 286-5810
Nona.K.Cheeks.1@gsfc.nasa.gov

Jet Propulsion Laboratory
Art Murphy, Jr.
(818) 354-3480
arthur.j.murphy-jr@jpl.nasa.gov

Johnson Space Center
Charlene E. Gilbert
(281) 483-3809
commercialization@jsc.nasa.gov

Kennedy Space Center
Jim Aliberti
(321) 867-6224
Jim.Aliberti-1@ksc.nasa.gov

Langley Research Center
Jesse Midgett
(757) 864-3936
jesse.c.midgett@nasa.gov

John H. Glenn Research Center at Lewis Field
Larry Viterna
(216) 433-3484
cto@grc.nasa.gov

Marshall Space Flight Center
Vernotto McMillan
(256) 544-2615
vernotto.mcmillan@msfc.nasa.gov

Stennis Space Center
Robert Bruce
(228) 688-1929
robert.c.bruce@nasa.gov

NASA Program Offices

At NASA Headquarters there are seven major program offices that develop and oversee technology projects of potential interest to industry:

Carl Ray
Small Business Innovation Research Program (SBIR) & Small Business Technology Transfer Program (STTR)
(202) 358-4652 or
cray@mail.hq.nasa.gov

Benjamin Neumann
InnovativeTechnology Transfer Partnerships (Code RP)
(202) 358-2320
benjamin.j.neumann@nasa.gov

John Mankins
Office of Space Flight (Code MP)
(202) 358-4659 or
jmankins@mail.hq.nasa.gov

Terry Hertz
Office of Aero-Space Technology (Code RS)
(202) 358-4636 or
thertz@mail.hq.nasa.gov

Glen Mucklow
Office of Space Sciences (Code SM)
(202) 358-2235 or
gmucklow@mail.hq.nasa.gov

Roger Crouch
Office of Microgravity Science Applications (Code U)
(202) 358-0689 or
rcrouch@hq.nasa.gov

Granville Paules
Office of Mission to Planet Earth (Code Y)
(202) 358-0706 or
gpaules@mtpe.hq.nasa.gov

TECH BRIEFS

NATIONAL AERONAUTICS AND SPACE ADMINISTRATION

Multisensor Instrument for Real-Time Biological Monitoring

Multiple parameters can be measured simultaneously by use of a single compact sensor head.

*Lyndon B. Johnson Space Center, Houston, Texas*

The figure schematically depicts an instrumentation system, called a "fiber optic-based integration system" (FOBIS), that is undergoing development to enable real-time monitoring of fluid cell cultures, bioprocess flows, and the like. The FOBIS design combines a micro flow cytometer (MFC), a microphotometer (MP), and a fluorescence-spectrum- or binding-force-measuring micro-sensor (MS) in a single instrument that is capable of measuring multiple biological parameters simultaneously or sequentially. The fiber-optic-based integration system is so named because the MFC, the MP, and the MS are integrated into a single optical system that is coupled to light sources and photometric equipment via optical fibers. The optical coupling components also include a wavelength-division multiplexer and diffractive optical elements. The FOBIS includes a laser-diode- and fiber-optic-based optical trapping subsystem ("optical tweezers") with microphotometric and micro-sensing capabilities for noninvasive confinement and optical measurement of relevant parameters of a single cell or other particle.

Some of the measurement techniques implemented together by the FOBIS have long been used separately to obtain basic understanding of the optical properties of individual cells and other organisms, the optical properties of populations of organisms, and the interrelationships among these properties, physiology of the organisms, and physical processes that govern the media that surround the organisms. For example, flow cytometry yields information on numerical concentrations, cross-sectional areas, and types of cells or other particles. Micro-sensing can be used to measure pH and concentrations of oxygen, carbon dioxide, glucose, metabolites, calcium, and antigens in a cell-culture fluid, thereby providing feedback that can be helpful in improving control over a bioprocess. Microphotometry (including measurements of scattering and fluorescence) can yield further information about optically trapped individual particles.

In addition to the multifunctionality not previously available in a single biological monitoring system, the FOBIS offers advantages of low mass, sensitivity, accuracy, portability, low cost, compactness (the overall dimensions of the fully developed FOBIS sensor head are expected to be less than 1 by 1 by 2 cm), and immunity to electromagnetic interference at suboptical frequencies. FOBIS could be useful in a variety of laboratory and field settings in such diverse endeavors as medical, veterinary, and general biological research; medical and veterinary diagnosis monitoring of industrial bioprocesses; and analysis of biological contaminants in air, water, and food.
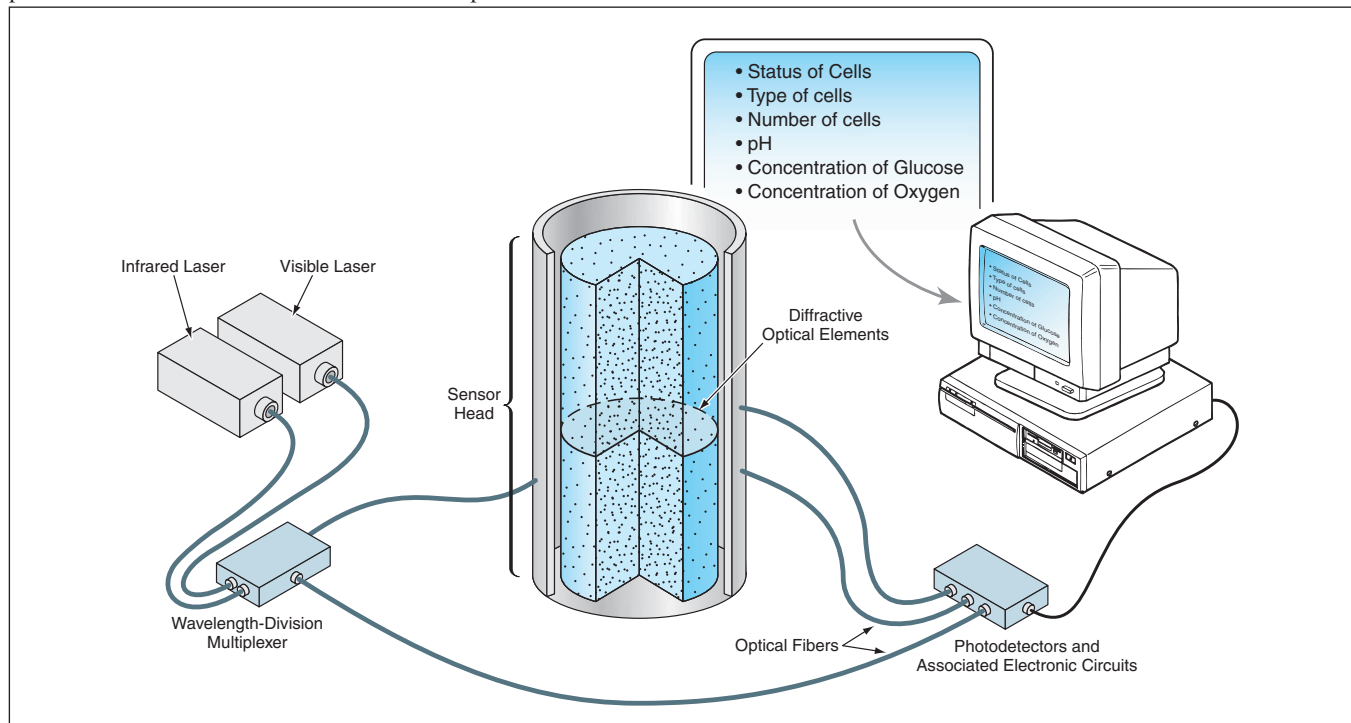
A **Compact Sensor Head** contains multiple optically coupled sensors that, together, yield a previously unavailable combination of real-time measurements of important parameters of cells, cell cultures, and cell-culture fluids.

Sensor for Monitoring Nanodevice-Fabrication Plasmas

Temperature and trace amounts of chemical species could be measured *in situ*.

Ames Research Center, Moffett Field, California

The term "plasma process diagnostics" (PPD) refers to a spectroscopic technique and sensing hardware that have been proposed for monitoring plasma processes used to fabricate electronic devices that feature sizes as small as several nanometers. Nanometer dimensions are characteristic of the quantum level of miniaturization, where single impurity atoms or molecules can drastically change the local properties of the nanostructures. Such changes may be purposely used in nanoscale design but may also be extremely damaging or cause improper operation of the fabricated devices. Determination of temperature and densities of reactants near the developing features is important, since the structural synthesis is affected by characteristics of the local microenvironment. Consequently, sensors capable of nonintrusive monitoring with high sensitivity and high resolution are essential for real-time atomistic control of reaction kinetics and minimizing trace contamination in plasma processes used to fabricate electronic nanodevices. Such process-monitoring sensors are required to be compact, multiparametric, and immune to the harsh environments of processing plasmas. PPD is intended to satisfy these requirements.

The specific technique used to implement plasma diagnostics with a PPD sensor would be an advanced version of continuous-wave cavity-ringdown spectroscopy (CW-CRDS) capable of profiling spectral line broadenings in order to derive both Doppler and Stark components. CRDS is based on measurements of the rate of absorption of laser light in an optical resonator. The ultimate sensitivity results from a very long absorption path length within the cavity and immunity to variations in incident laser intensity. The proposed version of this technique would involve the use of multiplexing tunable laser diodes and an actively modulated high-reflectivity optical resonator, thus offering a synergistic combination of simplicity, compactness, high sensitivity, and high resolution.

The multiplexing capabilities of diode lasers could be utilized to make the PPD sensor a single, simple, compact, and inexpensive tool for the acquisition of multiparametric data. A PPD sensor would be capable of continuous measurement of such physical parameters as gas temperature, gas velocity, electron number density, and absolute densities of reacting chemical species. A laser beam can be easily adjusted to analyze the immediate vicinity of the growing nanostructures (or features etched down) in real time. The absorption enhancement in an optical cavity would afford the sensitivity needed for measurement of the temperature and densities of species at concentrations significantly lower than measurable by other nonintrusive techniques.

It is anticipated that fully developed PPD sensors would enable simultaneous measurement of local temperature and determination of plasma species responsible for the synthesis and functionalization of nanodevices. These sensors would also enable tracking the pathways and origins of damaging contaminants, thereby providing feedback for adjustment of processes to optimize them and reduce contamination. The PPD sensors should also be useful for optimization of conventional microelectronics manufacturing plasma processes.

Going beyond plasma processes for fabrication of electronic devices, PPD sensors could be used for monitoring of atoms, molecules, ions, radicals, clusters, and particles in a variety of other settings, including outer space. Because of their high sensitivity, such sensors could also prove useful for detecting traces of illegal drugs and explosives.

Backed Bending Actuator

Such an actuator could exert a large force at small displacement.

Langley Research Center, Hampton, Virginia

Bending actuators of a proposed type would partly resemble ordinary bending actuators, but would include simple additional components that would render them capable of exerting large forces at small displacements. Like an ordinary bending actuator, an actuator according to the proposal would include a thin rectangular strip that would comprise two bonded layers (possibly made of electroactive polymers with surface electrodes) and would be clamped at one end in the manner of a cantilever beam. Unlike an ordinary bending actuator, the proposed device would include a rigid flat backplate that would support part of the bending strip against backward displacement; because of this feature, the proposed device is called a backed bending actuator.

When an ordinary bending actuator is inactive, the strip typically lies flat, the tip displacement is zero, and the force exerted by the tip is zero. During activation, the tip exerts a transverse force and undergoes a bending displacement that results from the expansion or contraction of one or more of the bonded layers. The tip force of an ordinary bending actuator is inversely proportional to its length; hence, a long actuator tends to be weak.

The figure depicts an ordinary bending actuator and the corresponding backed bending actuator. The bending, the tip displacement (d), and the tip force (F) exerted by the ordinary bending actuator are well approximated by the conventional equations for the loading and deflection of a cantilever beam subject to a bending moment which, in this case, is applied by the differential
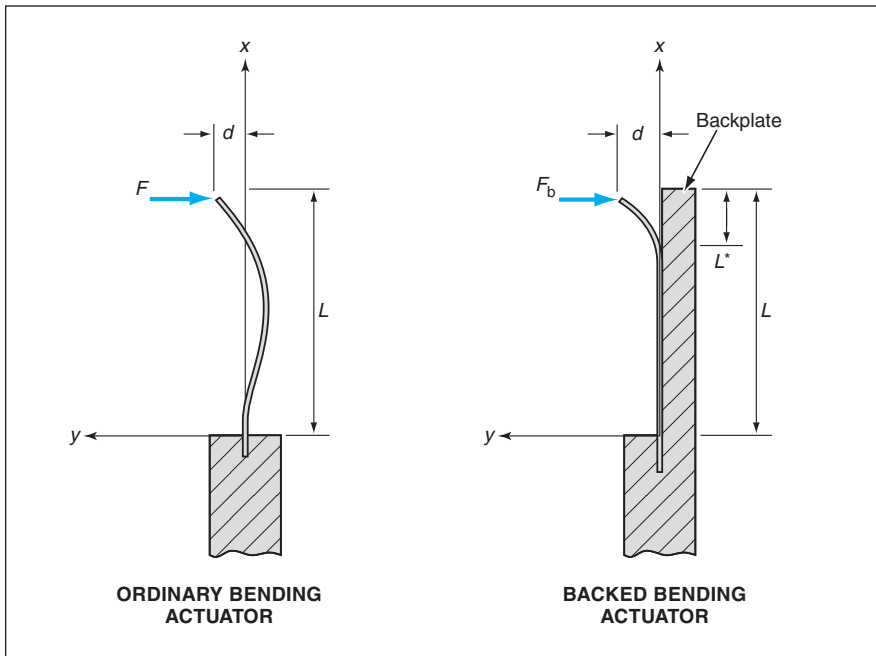
A **Backed Bending Actuator** would resemble an ordinary bending actuator except that it would include a backplate that would enable a large displacement together with a large force at small displacements.

expansion or contraction of the bonded layers. The bending, displacement, and tip force of the backed bending actuator are calculated similarly, except that it is necessary to account for the fact that the force F_b that resists the displacement of the tip could be sufficient to push part of the strip against the backplate; in such a condition, the cantilever beam would be effectively shortened (length L^*) and thereby stiffened and, hence, made capable of exerting a greater tip force for a given degree of differential expansion or contraction of the bonded layers.

Taking all of these effects into account, the cantilever-beam equations show that F_b would be approximately inversely proportional to $d^{1/2}$ for d less than a calculable amount, denoted the transition displacement (d_t). For $d < d_t$, part of the strip would be pressed against the backplate. Therefore, the force F_b would be very large for d at or near zero and would decrease as d increases toward d_t. At $d > d_t$, none of the strip would be pressed against the backplate and F_b would equal the tip force F of the corresponding ordinary bending actuator. The advantage of the proposal is that a backed bending actuator could be made long to obtain large displacement when it encountered little resistance but it could also exert a large zero-displacement force, so that it could more easily start the movement of a large mass, throw a mechanical switch, or release a stuck mechanism.

This work was done by Robert C. Costen and Ji Su of **Langley Research Center**. *Further information is contained in a TSP (see page 1)*
LAR-16441

Compact Optoelectronic Compass

The axis of rotation of the Earth is estimated from the changing direction to the Sun.

NASA's Jet Propulsion Laboratory, Pasadena, California

A compact optoelectronic sensor unit measures the apparent motion of the Sun across the sky. The data acquired by this chip are processed in an external processor to estimate the relative orientation of the axis of rotation of the Earth. Hence, the combination of this chip and the external processor finds the direction of true North relative to the chip: in other words, the combination acts as a solar compass. If the compass is further combined with a clock, then the combination can be used to establish a three-axis inertial coordinate system. If, in addition, an auxiliary sensor measures the local vertical direction, then the resulting system can determine the geographic position.

This chip and the software used in the processor are based mostly on the same design and operation as those of the unit described in "Micro Sun Sensor for Spacecraft" (NPO-30867) elsewhere in this issue of *NASA Tech Briefs*. Like the unit described in that article, this unit includes a small multiple-pinhole camera comprising a micromachined mask containing a rectangular array of microscopic pinholes mounted a short distance in front of an image detector of the active-pixel sensor
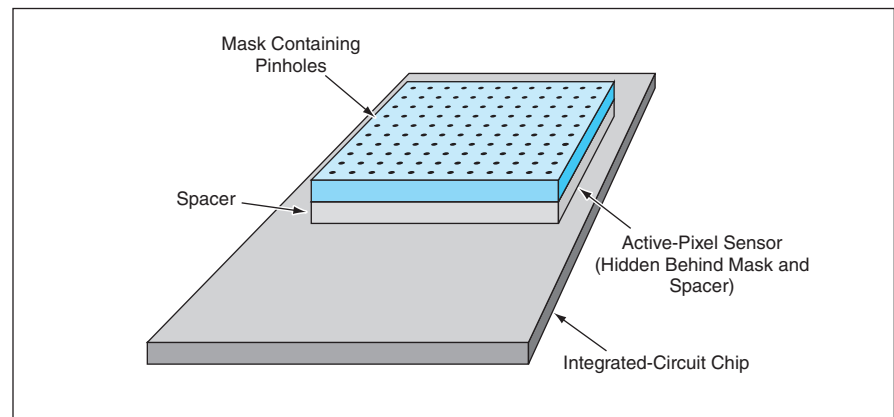
A **Compact Multiple-Pinhole Camera** senses the apparent position of the Sun and its apparent motion across the sky.

(APS) type (see figure). Further as in the other unit, the digitized output of the APS in this chip is processed to compute the centroids of the pinhole Sun images on the APS. Then the direction to the Sun, relative to the compass chip, is computed from the positions of the centroids (just like a sundial).

In the operation of this chip, one is interested not only in the instantaneous direction to the Sun but also in the apparent path traced out by the direction to the Sun as a result of rota-tion of the Earth during an observation interval (during which the Sun sensor must remain stationary with respect to the Earth). The apparent path of the Sun across the sky is projected on a sphere. The axis of rotation of the Earth lies at the center of the projected circle on the sphere surface. Hence, true North (not magnetic North), relative to the chip, can be estimated from paths of the Sun images across the APS.

In a test, this solar compass has been found to yield a coarse estimate of the North (within tens of degrees) in an observation time of about ten minutes. As expected, the accuracy was found to increase with observation time: after a few hours, the estimated direction of the rotation axis becomes accurate to within a small fraction of a degree.

Micro Sun Sensor for Spacecraft

NASA's Jet Propulsion Laboratory, Pasadena, California

A report describes the development of a compact micro Sun sensor for use as a part of the attitude determination subsystem aboard future miniature spacecraft and planetary robotic vehicles. The prototype unit has a mass of only 9 g, a volume of only 4.2 cm^3, a power consumption of only 30 mW, and a 120° field of view. The unit has demonstrated an accuracy of 1 arcminute. The unit consists of a multiple-pinhole camera: A micromachined mask containing a rectangular array of microscopic pinholes, machined utilizing the microelectromechanical systems (MEMS), is mounted in front of an active-pixel sensor (APS) image detector. The APS consists of a 512×512-pixel array, on-chip 10-bit analog to digital converter (ADC), on-chip bias generation, and on-chip timing control for self-sequencing and easy programmability. The digitized output of the APS is processed to compute the centroids of the pinhole Sun images on the APS. The Sun angle, relative to a coordinate system fixed to the sensor unit, is then computed from the positions of the centroids.

This work was done by Sohrab Mobasser, Carl Liebe, Youngsam Bae, Jeffrey Schroeder, and Chris Wrigley of Caltech for **NASA's Jet Propulsion Laboratory**. *Further information is contained in a TSP (see page 1)*
NPO-30867

Passive IFF: Autonomous Nonintrusive Rapid Identification of Friendly Assets
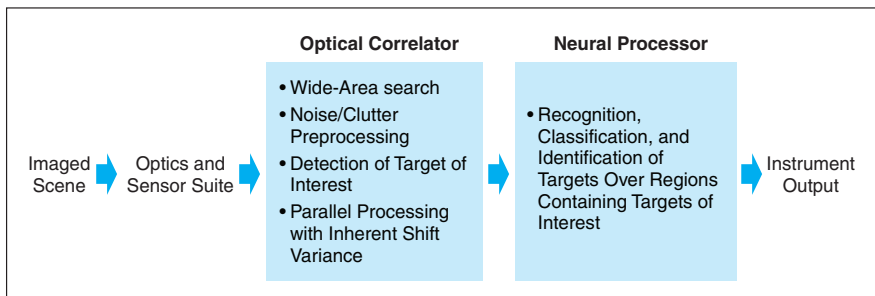### Targeting decisions could be made with speed needed in urgent situations.

NASA's Jet Propulsion Laboratory, Pasadena, California

A proposed optoelectronic instrument would identify targets rapidly, without need to radiate an interrogating signal, apply identifying marks to the targets, or equip the targets with transponders. The instrument was conceived as an identification, friend or foe (IFF) system in a battlefield setting, where it would be part of a targeting system for weapons, by providing rapid identification for aimed weapons to help in deciding whether and when to trigger them. The instrument could also be adapted to law-enforcement and industrial applications in which it is necessary to rapidly identify objects in view.

The instrument would comprise mainly an optical correlator and a neural processor (see figure). The inherent parallel-processing speed and capability of the optical correlator would be exploited to obtain rapid identification of a set of probable targets within a scene of interest and to define regions within the scene for the neural processor to analyze. The neural processor would then concentrate on each region selected by the optical correlator in an effort to identify the target. Depending on whether or not a target was recognized by comparison of its image data with data in an internal database on which the neural processor was trained, the processor would generate an identifying signal (typically, "friend" or "foe"). The time taken for this identification process would be less than the time needed by a human or robotic gunner to acquire a view of, and aim at, a target.

An optical correlator that has been under development for several years and that has been demonstrated to be capable of tracking a cruise missile might be considered a prototype of the optical correlator in the proposed IFF instrument. This optical correlator features a 512-by-512-pixel input image frame and operates at an input frame rate of 60 Hz. It includes a spatial light modulator (SLM) for video-to-optical image conversion, a pair of precise lenses to effect Fourier transforms, a filter SLM for digital-to-optical correlation-filter data conversion, and a charge-coupled device (CCD) for detection of correlation peaks. In operation, the input scene grabbed by a video sensor is streamed into the input SLM. Precomputed correlation-filter data files representative of known targets are then downloaded and sequenced into the filter SLM at a rate of 1,000 Hz. When there occurs a match between the input target data and one of the known-target data files, the CCD detects a correlation peak at the location of the target. Distortion-invariant correlation filters from a bank of such filters are then sequenced through the optical correlator for each input frame. The net result is the rapid preliminary recognition of one or a few targets.

		Optical Correlator	Neural Processor	
Imaged Scene	Optics and Sensor Suite	• Wide-Area search • Noise/Clutter Preprocessing • Detection of Target of Interest • Parallel Processing with Inherent Shift Variance	• Recognition, Classification, and Identification of Targets Over Regions Containing Targets of Interest	Instrument Output

An **Optical Correlator and a Neural Processor**, each performing a different portion of the overall target-identification task, would generate a signal indicative of the identity of a target (e.g., "friend" or "foe") in a fraction of a second.

The output of the optical correlator would be fed to the neural processor for classification and identification of the preliminarily recognized targets. The neural processor could contain one or more analog and/or digital artificial neural networks, which are well suited for identification of targets by virtue of their fault tolerance and their capabilities for adaptation, classification of patterns, and complex learning. An analog neural processor with a parallel configuration that has been demonstrated to be capable of classifying hyperspectral images and patterns may be suitable as a prototype neural processor for this instrument.

Finned-Ladder Slow-Wave Circuit for a TWT

Impedance and gain per unit length are increased.

John H. Glenn Research Center, Cleveland, Ohio

A finned-ladder structure has been invented in an effort to improve the design of the slow-wave circuit of a traveling-wave tube (TWT). The point of departure for the design effort was a prototype TWT that contains a ring-plane slow-wave circuit (see Figure 1). The design effort was a response to the observation that despite the high-power capabilities of the ring-plane TWT, its requirement for a high supply voltage and its low bandwidth have made it unacceptable for use outside a laboratory setting.

Modifications of the ring-plane slow-wave circuit were proposed on the basis of the physics of interaction of the electromagnetic field with this circuit and with the electron beam. The effects of each proposed modification were analyzed by use of the Solution of Maxwell's Equations by the Finite-Integration-Algorithm (MAFIA) computer program — a powerful, modular electromagnetic-simulation code for the computer-aided design and analysis of two- and three-dimensional electromagnetic devices, including magnets, radio-frequency cavities, waveguides, and antennas. For each trial design, MAFIA was used to calculate frequency-vs.-phase dispersion characteristics, and attenuation and small-signal gain vs. frequency. Also calculated were values of the beam on-axis interaction impedance, which is a measure of the strength of interaction between a radio-frequency wave and the electron beam. A nominal operating frequency of 32 GHz was used in the design calculations and numerical simulations of performance.

The modifications that were adopted included an increase in the inner diameter of the outer barrel, introduction of slots into the planes that support the rings, and the addition of metal loading fins. Figure 2 depicts the finned-ladder slow-wave structure that was adopted as a result of the iterated modifications and computations.
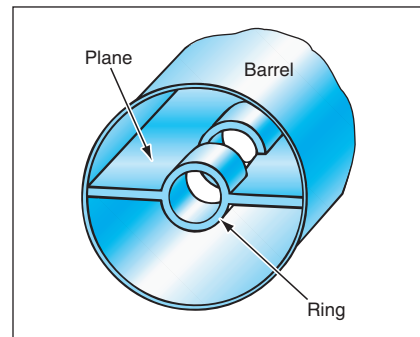

Figure 1. A **Prototype Ring-Plane Circuit** was modified to obtain a finned-ladder circuit.

The simulations showed that the finned-ladder structure can be expected to exhibit radio-frequency output power of 20 W (corresponding to efficiency of 20.2 percent) and on-axis interaction impedance of 120 Ω at an applied potential of 6.8 kV and nominal operating frequency of 32 GHz, with a half-power bandwidth of greater than 3 percent. The computed gain, efficiency, and on-axis interaction impedance are greater than those of prior TWTs that contain helical and coupled-cavity slow-wave structures, and the applied potential is low, relative to that of a TWT containing a ring-plane slow-wave structure. Moreover, because of the greater gain per unit length of the finned-ladder structure (relative to helical and coupled-cavity structures), slow-wave circuits needed to obtain a given amount of gain could be made significantly shorter.

The overall dimensions of the designed the finned-ladder structure are a diameter of 0.093 in. (2.36 mm) and length of 2 in. (50.8 mm). Because of their smallness, it would not be possible to fabricate the disks of the finned-ladder structure by conventional machining. Instead, it has been proposed to fabricate them by batch chemical milling and/or micro-electrical-discharge
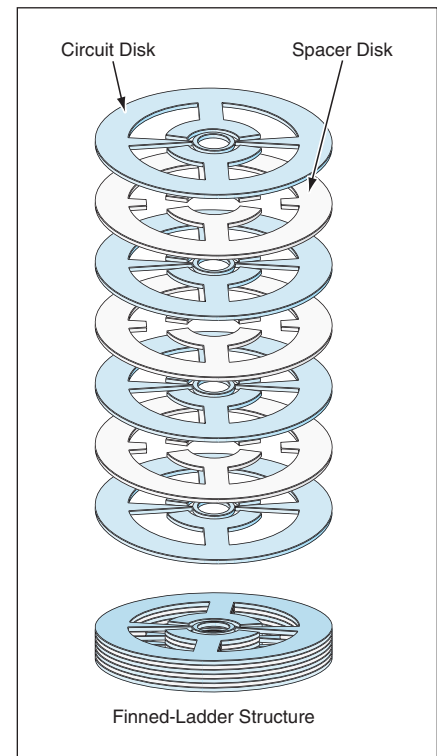

Figure 2. A **Finned-Ladder Circuit** has an all-metal structure comprising circuit and spacer disks. Numerical simulations show that the finned-ladder circuit offers advantages over prior slow-wave circuits.

machining. The circuit and spacer disks would be stacked alternately and diffusion-bonded to form the all-metal periodic finned-ladder circuit structure.

Directional Radio-Frequency Identification Tag Reader

John F. Kennedy Space Center, Florida

A directional radio-frequency identification (RFID) tag reader has been designed to facilitate finding a specific object among many objects in a crowded room. The device could be an adjunct to an electronic inventory system that tracks RFID-tagged objects as they move through reader-equipped doorways. Whereas commercial RFID-tag readers do not measure directions to tagged objects, the device is equipped with a phased-array antenna and a received-signal-strength indicator (RSSI) circuit for measuring direction. At the beginning of operation, it is set to address only the RFID tag of interest. It then continuously transmits a signal to interrogate that tag while varying the radiation pattern of the antenna. It identifies the direction to the tag as the radiation-pattern direction of peak strength of the signal returned by the tag. An approximate distance to the tag is calculated from the peak signal strength. The direction and distance can be displayed on a screen. A prototype containing a Yagi antenna was found to be capable of detecting a 915.5-MHz tag at a distance of ≈15 ft (≈4.6 m).

This work was done by Pedro J. Medelius, John D. Taylor, and John J. Henderson of Dynacs, Inc., for **Kennedy Space Center**.

Integrated Solar-Energy-Harvesting and -Storage Device

Efficiency would be maximized for anticipated ranges of operating conditions.

NASA's Jet Propulsion Laboratory, Pasadena, California

A modular, integrated, completely solid-state system designed to harvest and store solar energy is under development. Called the "power tile," the hybrid device consists of a photovoltaic cell, a battery, a thermoelectric device, and a charge-control circuit that are heterogeneously integrated to maximize specific energy capacity and efficiency. Power tiles could be used in a variety of space and terrestrial environments and would be designed to function with maximum efficiency in the presence of anticipated temperatures, temperature gradients, and cycles of sunlight and shadow. Because they are modular in nature, one could use a single power tile or could construct an array of as many tiles as needed. If multiple tiles are used in an array, the distributed and redundant nature of the charge control and distribution hardware provides an extremely fault-tolerant system.

The figure presents a schematic view of the device. High-efficiency photovoltaic cells would be attached to a thin-film array of thermoelectric devices, which, in turn, would be integrated to a multi-layer thin-film solid-state battery packaged in a thermally conductive envelope. The charge control circuitry would be integrated either onto the battery side of the device or into a protective frame that would enclose the device. The entire package is designed to be less than 2 mm thick.

The thermoelectric devices would harvest some of the thermal energy incurred when solar radiation raises the temperature on the photovoltaic-cell side relative to the shaded backside. The battery would be placed on that opposite side, and the outer surface of its thermally conductive envelope would be coated with a thermally emissive material to aid in creating the greatest possible temperature differential for optimum operation of the thermoelectric device. The same thermoelectric devices could also be operated in a power-consuming, heat-pump mode to keep the batteries within a desired operational temperature range during intervals of darkness/cold. Microthermoelectric devices that are no more than 500 μm thick are currently under fabrication for intended integration into the power tile device.

The solid-state battery system performs nominally in the temperature range of –20 to 60 °C, and has been shown to function at limited discharge rates to temperatures as low as –40 °C. These thin-film solid-state cells, based on mate-
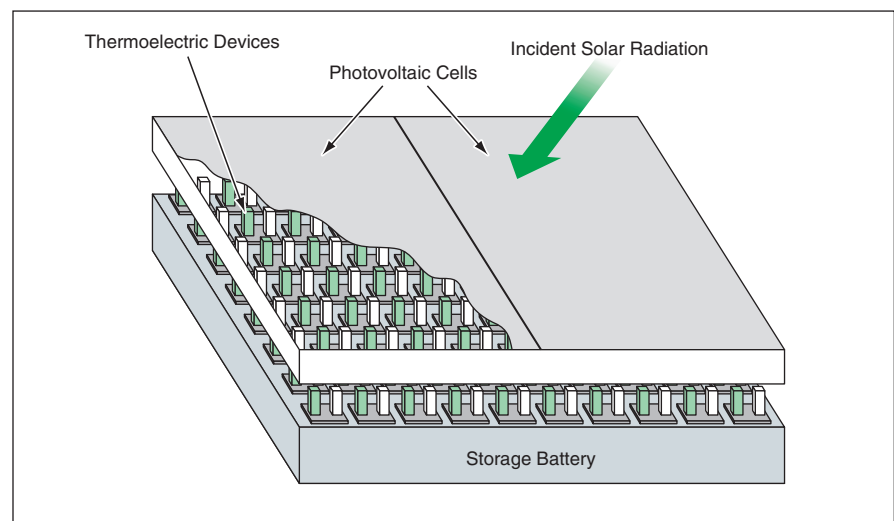
A **Power Tile** would include energy-harvesting, energy-storing, and temperature-regulating parts integrated into a compact package.

rials systems originally developed at Oak Ridge National Laboratories in the 1990's, are capable of over 30,000 charge/discharge cycles without appreciable capacity fade, and can withstand intermittent heating and cooling to temperatures above 100 °C and below –40 °C.

To achieve high efficiency, the photovoltaic, thermoelectric device and the microbattery need to operate coherently. A smart power silicon chip, currently under development at JPL, will ensure the coherent operation of the energy generating and storage devices within the power tile system. This chip includes three synchronized high-efficiency DC-DC voltage converters for producing common voltage from the three sources, a battery-charging circuit, a thermoelectric heater driver circuit, and all the necessary sense and control circuits to produce the synchronized operation.

A prototype power tile, fabricated at JPL, has dimensions of 3 cm by 3 cm by 3 mm. The dual-junction photovoltaic cell in this power tile is capable of delivering a current of 125 mA at a potential of 2.1 V in full sunlight (1 AU). The thermoelectric device, a commercial off-the-shelf system 1.9 mm thick, generates a current of 20 mA at a potential of approximately 0.8 V when the photovoltaic side is at a temperature of 80 °C and the storage-battery side at a temperature of 45 °C. The battery is a 1 mm thick Li/LiPON/LiCoO solid-state multilayer system capable of delivering 20 – 50 mW of power during the 1/2 hour of ellipse time typically encountered in low Earth orbit. The photovoltaic cells and thermoelectric devices are integrated using a thermally conductive silver epoxy, while the battery is encased in aluminum. The power tile has been tested in an X-25 solar simulator and has been shown to function in a variety of conditions. Ongoing work includes miniaturizing the charge control electronics, integrating true microthermoelectric devices, and extended lifetime testing.

Event-Driven Random-Access-Windowing CCD Imaging System

Regions of interest can be adapted to changes in the scene.

NASA's Jet Propulsion Laboratory, Pasadena, California

A charge-coupled-device (CCD) based high-speed imaging system, called a real-time, event-driven (RARE) camera, is undergoing development. This camera is capable of readout from multiple subwindows [also known as regions of interest (ROIs)] within the CCD field of view. Both the sizes and the locations of the ROIs can be controlled in real time and can be changed at the camera frame rate. The predecessor of this camera was described in "High-Frame-Rate CCD Camera Having Subwindow Capability" (NPO-30564) *NASA Tech Briefs*, Vol. 26, No. 12 (December 2002), page 26. The architecture of the prior camera requires tight coupling between camera control logic and an external host computer that provides commands for camera operation and processes pixels from the camera. This tight coupling limits the attainable frame rate and functionality of the camera.

The design of the present camera loosens this coupling to increase the achievable frame rate and functionality. From a host computer perspective, the readout operation in the prior camera was defined on a per-line basis; in this camera, it is defined on a per-ROI basis. In addition, the camera includes internal timing circuitry. This combination of features enables real-time, event-driven operation for adaptive control of the camera. Hence, this camera is well suited for applications requiring autonomous control of multiple ROIs to track multiple targets moving throughout the CCD field of view. Additionally, by eliminating the need for control intervention by the
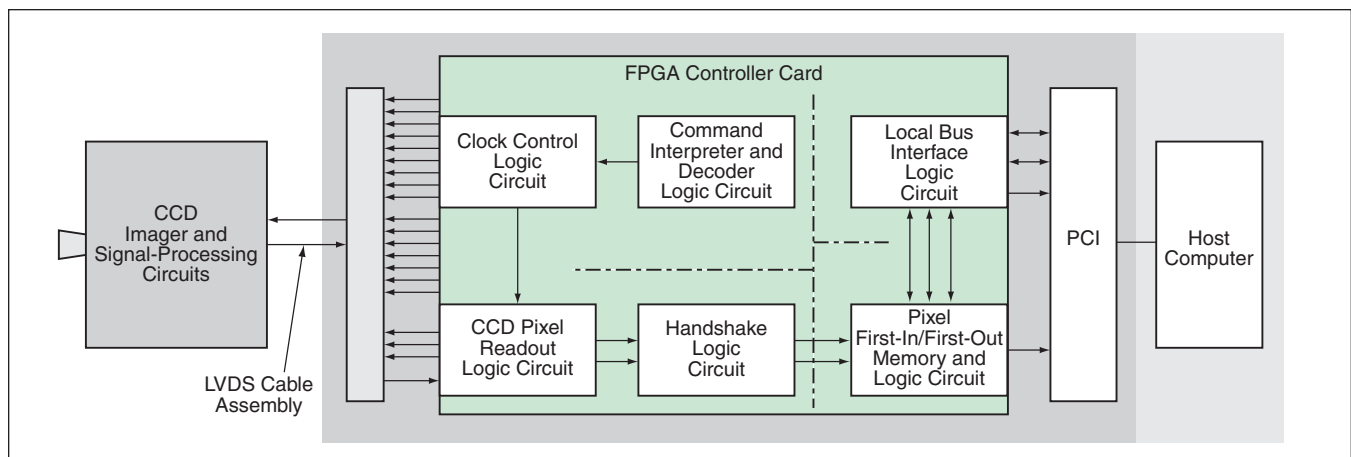
The **RARE Camera** is a high-speed CCD-based imaging system that offers enhanced speed and functionality for tracking moving targets.

host computer during the pixel readout, the present design reduces ROI-readout times to attain higher frame rates.

This camera (see figure) includes an imager card consisting of a commercial CCD imager and two signal-processor chips. The imager card converts transistor/transistor-logic (TTL)-level signals from a field programmable gate array (FPGA) controller card. These signals are transmitted to the imager card via a low-voltage differential signaling (LVDS) cable assembly. The FPGA controller card is connected to the host computer via a standard peripheral component interface (PCI). The host computer sends control parameters to the FPGA controller card and reads camera-status and pixel data from the FPGA controller card. Some of the operational parameters of the camera are programmable in hardware. Commands are loaded from the host computer into the FPGA controller card to define such parameters as the frame rate, integration time, and the size and location of an ROI.

There are two modes of operation: image capture and ROI readout. In image-capture mode, whole frames of pixels are repeatedly transferred from the image area to the storage area of the CCD, with timing defined by the frame rate and integration time registers loaded into the FPGA controller card. In ROI readout, the host computer sends commands to the FPGA controller specifying the size and location of an ROI in addition to the frame rate and integration time. The commands result in scrolling through unwanted lines and through unwanted pixels on lines until pixels in the ROI are reached. The host computer can adjust the sizes and locations of the ROIs within a frame period for dynamic control to changes in the image (e.g., for tracking targets).

Stroboscope Controller for Imaging Helicopter Rotors

This unit can be programmed to operate in a variety of configurations.

Ames Research Center, Moffett Field, California

A versatile electronic timing-and-control unit, denoted a rotorcraft strobe controller, has been developed for use in controlling stroboscopes, lasers, video cameras, and other instruments for capturing still images of rotating machine parts — especially helicopter rotors. This unit is designed to be compatible with a variety of sources of input shaft-angle or timing signals and to be capable of generating a variety of output signals suitable for triggering instruments characterized by different input-signal specifications. It is also designed to be flexible and reconfigurable in that it can be modified and updated through changes in its control software, without need to change its hardware.

Figure 1 is a block diagram of the rotorcraft strobe controller. The control processor is a high-density complementary metal oxide semiconductor, single-chip, 8-bit microcontroller. It is connected to a 32K × 8 nonvolatile static random-access memory (RAM) module. Also connected to the control processor is a 32K × 8 electrically programmable read-only-memory (EPROM) module, which is used to store the control software. Digital logic support circuitry is implemented in a field-programmable gate array (FPGA). A 240 × 128-dot, 40-character × 16-line liquid-crystal display (LCD) module serves as a graphical user interface; the user provides input through a 16-key keypad mounted next
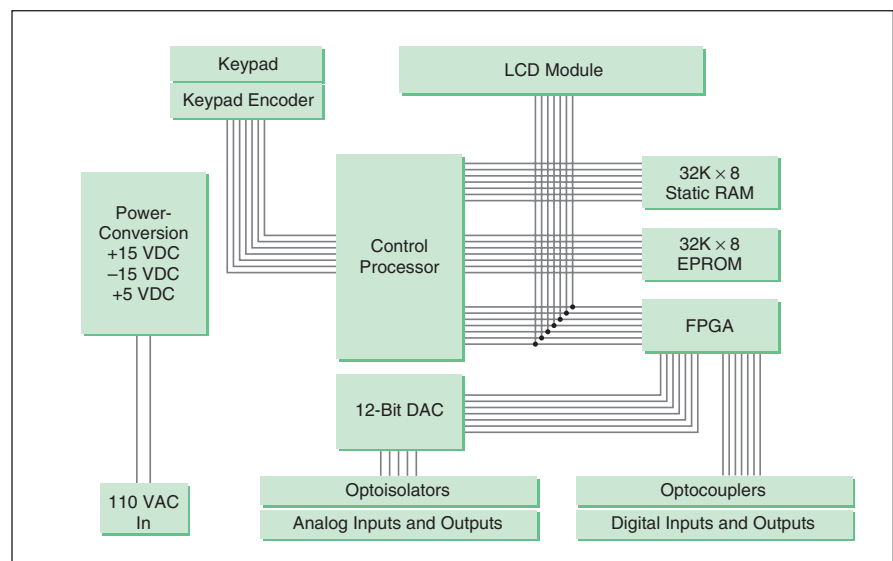
Figure 1. The **Control Processor Is Controlled by Software** that resides in the EPROM. The functionality of the system can be modified via the software, without changing the hardware.

to the LCD. A 12-bit digital-to-analog converter (DAC) generates a 0-to-10-V ramp output signal used as part of a rotor-blade monitoring system, while the control processor generates all the appropriate strobing signals. Optocouplers are used to isolate all input and output digital signals, and optoisolators are used to isolate all analog signals.

The unit is designed to fit inside a 19-in. (≈48-cm) rack-mount enclosure. Electronic components are mounted on a custom printed-circuit board (see Figure 2). Two power-conversion modules on the printed-circuit board convert AC power to +5 VDC and ±15 VDC, respectively. Located on the back of the unit are 16 bayonet connectors used for input and output. There are 14 outputs: 10 analog voltage ramp waveforms, a once-per-revolution pulse, an *n*-times-per-revolution (where *n* is an integer selectable by the user) pulse, a transistor/transistor logic (TTL) digital strobe signal, and an open-collector digital strobe signal. There are two input connectors which accept a TTL once-per-revolution and an *n*-per-revo-
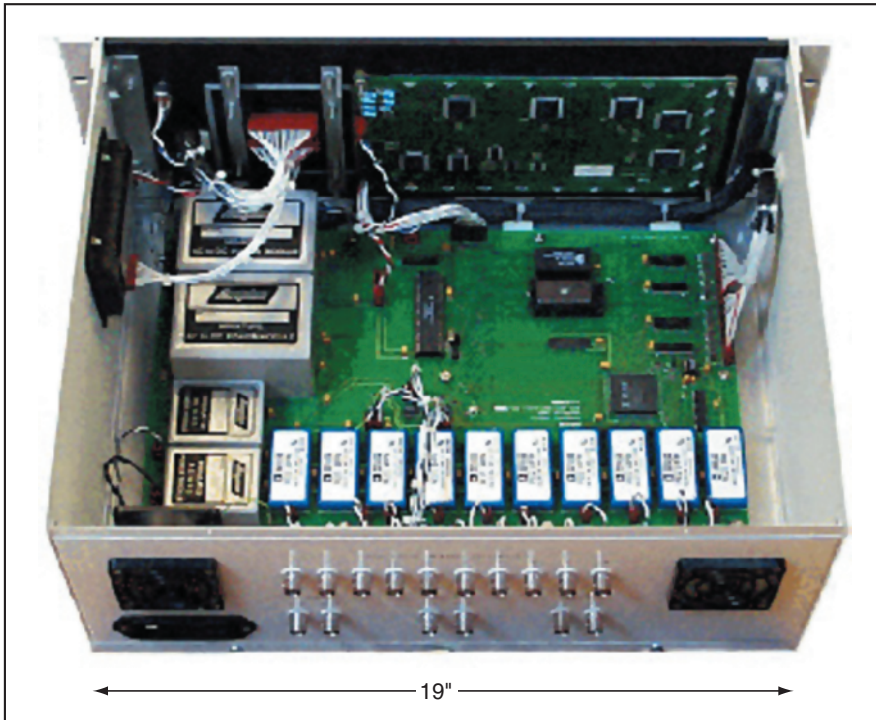
Figure 2. The **Rack-Mount Enclosure** was photographed from above and behind with the cover removed to show components mounted on the printed-circuit board.

lution signal. They can be either single-ended, floating, or differential.

The control software was written in the C language. The main functions of the software are to read data present on the control-processor ports, generate the strobe signals, generate the ramp information used to monitor rotor-blade parameters by writing to the 12-bit DAC, save and retrieve configuration settings to and from the nonvolatile RAM, communicate with the FPGA, accept keypad input, and control and update the LCD by paging though appropriate user selections and menus. The user can gain access to several menus to set such parameters as the number of blades to track, the blade-offset angle, and the number of pulses per revolution.

This work was completed for Jon Lauten-schlager of the U.S. Army Aviation and Missile Command by Scott Jensen, John Marmie, and Nghia Mai of **Ames Research Center**. *Further information is contained in a TSP (see page 1)*

Inquiries concerning rights for the commercial use of this invention should be addressed to the Patent Counsel, Ames Research Center, (650) 604-5104. Refer to ARC-14966.

Software

Software for Checking Statecharts

HiVy is a software tool set that enables verification through model checking of designs represented as finite-state machines or statecharts. HiVy provides automated translation of (1) statecharts created by use of the MathWorks Stateflow® program to (2) Promela, the input language of the Spin model checker, which can then be used to verify, or trace logical errors in, distributed software systems. HiVy can operate directly on Stateflow models, or its abstract syntax of hierarchical sequential automata (HSA) can be used independently as an intermediate format for translation to Promela. In a typical design application, HiVy parses and reformats Stateflow model file data using the programs *SfParse* and *sf2hsa*, respectively. If the parsing effort is successful, an abstract syntax tree is delivered into a file named with the extension ".hsa." If the design comprises several model files, they may be merged into one ".hsa" file before translation into Promela. Stateflow scope is preserved, and name clashes are avoided in the merge process. The HiVy program *hsa2pr* translates the model from the intermediate HSA format into Promela. Additionally, HiVy provides through translation a list of all statechart model propositions that are the means for formalizing linear temporal logic (LTL) properties about the model for Spin verification.

This tool set was written by Paula Pingree of Caltech/JPL and Erich Mikk (independent consultant) for **NASA's Jet Propulsion Laboratory**. *Further information is contained in a TSP (see page 1)*

This software is available for commercial licensing. Please contact Don Hart of the California Institute of Technology at (818) 393-3425. Refer to NPO-30847.

Program Predicts Broadband Noise From a Turbofan Engine

Broadband Fan Noise Prediction System (BFaNS) is a computer program that, as its name indicates, predicts the broadband noise generated by the fan stage of a turbofan engine. This noise is the sum of (1) turbulent-inflow noise, which is caused by turbulence impinging on leading edges of the fan and the fan exit guide vane and (2) self noise, which is caused by turbulence convecting past the corresponding trailing edges. The user provides input data on the fan-blade, vane, and flow-path geometries and on the mean and turbulent components of the flow field. BFaNS then calculates the turbulent-inflow noise by use of D. B. Hanson's theory, which relates sound power to the inflow turbulence characteristics and the cascade geometry. Hanson's program, BBCASCADE, is incorporated into BFaNS, wherein it is applied to the rotor and stator in a stripwise manner. The spectra of upstream and downstream sound powers radiated by each strip are summed to obtain the total upstream and downstream sound-power spectra. The self-noise contributions are calculated by S. A. L. Glegg's theory, which is also applied in a stripwise manner. The current version of BFaNS is limited to fans with subsonic tip speeds.

This program was written by Bruce L. Morin of United Technologies for **Glenn Research Center**. *Further information is contained in a TSP (see page 1)*

Inquiries concerning rights for the commercial use of this invention should be addressed to NASA Glenn Research Center, Commercial Technology Office, Attn: Steve Fedor, Mail Stop 4–8, 21000 Brookpark Road, Cleveland, Ohio 44135. Refer to LEW-17307.

Protocol for a Delay-Tolerant Data-Communication Network

As its name partly indicates, the Delay-Tolerant Networking (DTN) Bundle Protocol is a protocol for delay-tolerant transmission of data via communication networks. This protocol was conceived as a result of studies of how to adapt Internet protocols so that Internet-like services could be provided across interplanetary distances in support of deep-space exploration. The protocol, and software to implement the protocol, is being developed in collaboration among experts at NASA's Jet Propulsion Laboratory and other institutions. No current Internet protocols can accommodate long transmission delay times or intermittent link connectivity. The DTN Bundle Protocol represents a departure from the standard Internet assumption that a continuous path is available from a host computer to a client computer: It provides for routing of data through networks that may be disjointed and may be characterized by long transmission delays. In addition to networks that include deep-space communication links, examples of such networks include terrestrial ones within which branches are temporarily disconnected. The protocol is based partly on the definition of a message-based overlay above the transport layers of the networks on which it is hosted.

This work was done by Jordan Torgerson, Adrian Hooke, Scott Burleigh, and Kevin Fall of Caltech for **NASA's Jet Propulsion Laboratory**. *Further information is contained in a TSP (see page 1)*

This software is available for commercial licensing. Please contact Don Hart of the California Institute of Technology at (818) 393-3425. Refer to NPO-35169.

Software Implements a Space-Mission File-Transfer Protocol

CFDP is a computer program that implements the CCSDS (Consultative Committee for Space Data Systems) File Delivery Protocol, which is an international standard for automatic, reliable transfers of files of data between locations on Earth and in outer space. CFDP administers concurrent file transfers in both directions, delivery of data out of transmission order, reliable and unreliable transmission modes, and automatic retransmission of lost or corrupted data by use of one or more of several lost-segment-detection modes. The program also implements several data-integrity measures, including file checksums and optional cyclic redundancy checks for each protocol data unit. The metadata accompanying each file can include messages to users' application programs and commands for operating on remote file systems.

This program was written by Kathleen Rundstrom, Son Q. Ho, Michael Levesque, Felicia Sanders, Scott Burleigh, and John Veregge of Caltech for **NASA's Jet Propulsion Laboratory**. *Further information is contained in a TSP (see page 1)*

This software is available for commercial licensing. Please contact Don Hart of the California Institute of Technology at (818) 393-3425. Refer to NPO-40247.

Making Carbon-Nanotube Arrays Using Block Copolymers: Part 2

A nanoscale phase separation would be utilized to form regularly spaced catalytic dots.

NASA's Jet Propulsion Laboratory, Pasadena, California

Some changes have been incorporated into a proposed method of manufacturing regular arrays of precisely sized, shaped, positioned, and oriented carbon nanotubes. Such arrays could be useful as mechanical resonators for signal filters and oscillators, and as electrophoretic filters for use in biochemical assays.

A prior version of the method was described in "Block Copolymers as Templates for Arrays of Carbon Nanotubes," (NPO-30240), *NASA Tech Briefs*, Vol. 27, No. 4 (April 2003), page 56. To recapitulate from that article:

As in other previously reported methods, carbon nanotubes would be formed by decomposition of carbon-containing gases over nanometer-sized catalytic metal particles that had been deposited on suitable substrates. Unlike in other previously reported methods, the catalytic metal particles would not be so randomly and densely distributed as to give rise to thick, irregular mats of nanotubes with a variety of lengths, diameters, and orientations. Instead, in order to obtain regular arrays of spaced-apart carbon nanotubes as nearly identical as possible, the catalytic metal particles would be formed in predetermined regular patterns with precise spacings. The regularity of the arrays would be ensured by the use of nanostructured templates made of block copolymers.

A block copolymer consists of two or more sections, or "blocks," each of which consists of a tailored number of monomers of a given type linked together as in a normal polymer molecule. Some combinations of monomers (for example, styrene and methylmethacrylate) yield block copolymer molecules that, under appropriate conditions, undergo a nanoscale phase separation in which they assemble themselves into repeating structures with unit-cell dimensions that typically range between 5 and 100 nm. In other words, a block copolymer can be made to acquire a regular structure on a length scale substantially larger than the individual monomer units yet well below a macroscopic scale.

Proposed techniques for utilizing such nanostructured block copolymers as templates are generally oriented toward exploiting the differences between chemical and/or physical properties of the different materials in the adjacent nanoscale regions (for example, the hydrophilicity of the methylmethacrylate blocks and the hydrophobicity of the styrene blocks). In the version of the method described in the cited previous article, one would utilize the differences in chemical reactivities of the blocks in order to selectively remove the blocks of PMMA, without removing the adjacent blocks of the other polymer, in order to create voids into which catalytic metals could be deposited. In the present version of the method, one would exploit differences in chemical reactivities in a different way, as described below.

In the present version (see figure), one would begin by dissolving a PS/PMMA diblock copolymer with an ionic salt of a suitable catalytic metal (e.g., $FeCl_3$) in a suitable amphiphilic solvent (e.g., acetone). The solution would be spin-coated onto a substrate, then heated so that the PS/PMMA block copolymer would form itself into pillars of PMMA in a PS matrix. During the heating, the Fe^{3+} and Cl^- would be expected to migrate to the PMMA regions, wherein the local dipoles in the oxygen-containing moieties would tend to attract and bind the ions. The resulting block copolymer film would contain a regular array of iron-rich and iron free regions with nanometer dimensions. The polymer would then be oxidized away by heating to a temperature of 400 °C in air, leaving a regular array of nearly identically sized and shaped iron oxide dots on the substrate. The substrate and dots would be heated in hydrogen to reduce the iron oxide dots to iron. Thereafter, carbon nanotubes would be grown on the iron dots as described above.
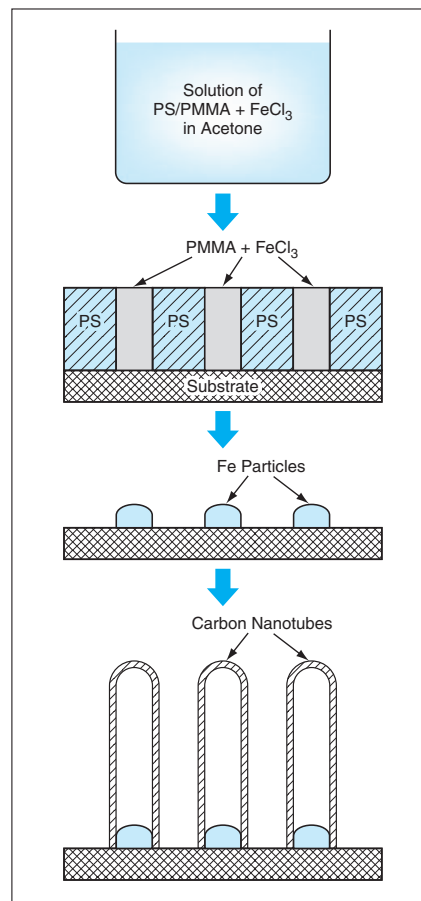
Regularly Spaced Fe Particles would be formed at the end of a process that would exploit the tendency of Fe+ ions to become bound in the PMMA blocks of a PS/PMMA block copolymer. The Fe particles would catalyze the growth of carbon nanotubes.

☢ Modular Rake of Pitot Probes

Individual probes can be replaced more easily than was possible before.

John H. Glenn Research Center, Cleveland, Ohio

The figure presents selected views of a modular rake of 17 pitot probes for measuring both transient and steady-state pressures in a supersonic wind tunnel. In addition to pitot tubes visible in the figure, the probe modules contain (1) high-frequency dynamic-pressure transducers connected through wires to remote monitoring circuitry and (2) flow passages that lead to tubes that, in turn, lead to remote steady-state pressure transducers.

Prior pitot-probe rakes were fabricated as unitary structures, into which the individual pitot probes were brazed. Repair or replacement of individual probes was difficult, costly, and time-consuming because (1) it was necessary to remove entire rakes in order to unbraze individual malfunctioning probes and (2) the heat of unbrazing a failed probe and of brazing a new probe in place could damage adjacent probes. In contrast, the modules in the present probe are designed to be relatively quickly and easily replaceable with no heating and, in many cases, without need for removal of the entire rake from the wind tunnel.

To remove a malfunctioning probe, one first removes a screw-mounted V-cross-section cover that holds the probe and adjacent probes in place. Then one removes a screw-mounted cover plate to gain access to the steady-state pressure tubes and dynamic-pressure wires. Next, one disconnects the tube and wires of the affected probe. Finally, one installs a new probe in the reverse of the aforementioned sequence.

The wire connections can be made by soldering, but to facilitate removal and installation, they can be made via miniature plugs and sockets. The connections between the probe flow passages and the tubes leading to the remote pressure sensors can be made by use of any of a variety of readily available flexible tubes that can be easily pulled off and slid back on for removal and installation, respectively.

This work was done by Timothy A. Dunlap of **Glenn Research Center**, *Michael W. Henry of QSS Group, Inc., and Raymond P. Homyk of Zin Technologies. Further information is contained in a TSP (see page 1)*

Inquiries concerning rights for the commercial use of this invention should be addressed to NASA Glenn Research Center, Commercial Technology Office, Attn: Steve Fedor, Mail Stop 4–8, 21000 Brookpark Road, Cleveland, Ohio 44135. Refer to LEW-17272.
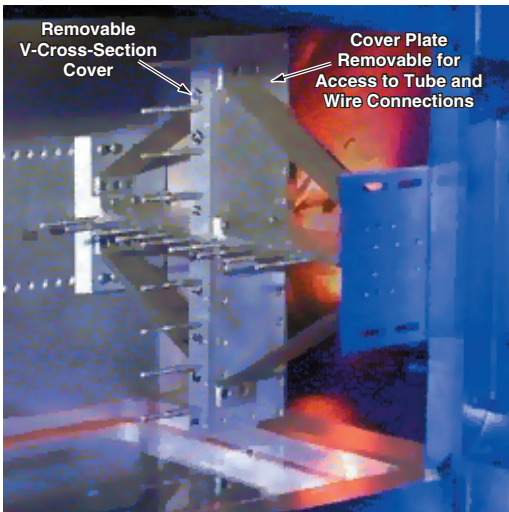
RAKE INSTALLED IN WIND TUNNEL   ENLARGED VIEW OF PART OF RAKE WITH COVER LIFTED OFF
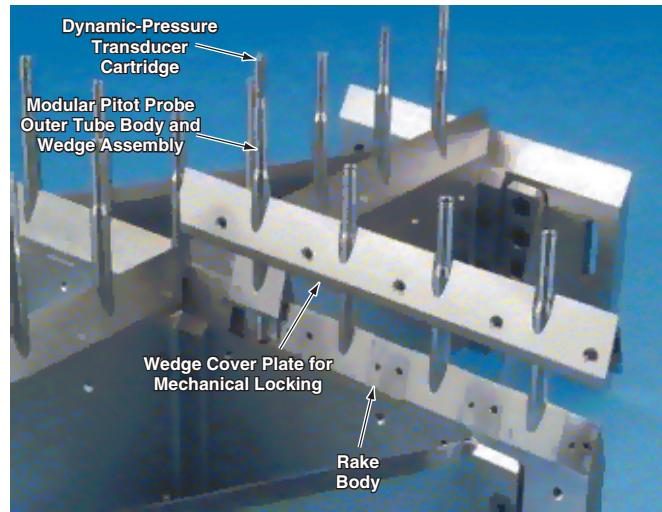
Each Probe Module in this probe rake is held in place by a wedge bracket under a V-cross-section cover plate. The wires and tube for connection to each probe are reached by removing one of the flat access cover plates.

☢ Preloading To Accelerate Slow-Crack-Growth Testing

Testing time can be reduced substantially with little effect on results.

John H. Glenn Research Center, Cleveland, Ohio

An accelerated-testing methodology has been developed for measuring the slow-crack-growth (SCG) behavior of brittle materials. Like the prior methodology, the accelerated-testing methodology involves dynamic fatigue ("constant-stress-rate") testing, in which a load or a displacement is applied to a specimen at a constant rate. SCG parameters or life-prediction parameters needed for designing components made of the same material as that of the specimen are cal-

Figure 1. **Applied Load or Stress** is increased linearly with time in dynamic fatigue testing. In the conventional approach, one starts from zero applied stress. In accelerated testing, one starts from a preload stress that is a significant fraction of the strength of the material.
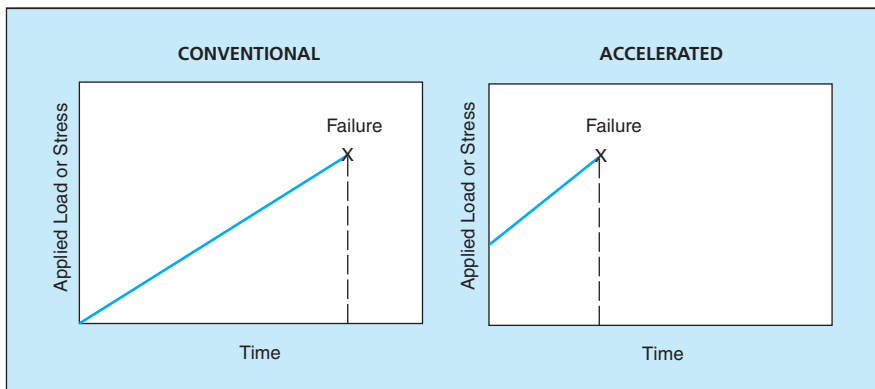

Figure 2. **The Effect of Preloading** on the normalized strength of a specimen as measured in a dynamic fatigue test has been computed for materials having several different values of n, a crack-growth parameter.

culated from the relationship between (1) the strength of the material as measured in the test and (2) the applied-stress rate used in the test. Despite its simplicity and convenience, dynamic fatigue testing as practiced heretofore has one major drawback: it is extremely time-consuming, especially at low stress rates.

The present accelerated methodology reduces the time needed to test a specimen at a given rate of applied load, stress, or displacement. Instead of starting the test from zero applied load or displacement as in the prior methodology, one preloads the specimen and increases the applied load at the specified rate (see Figure 1).

One might expect the preload to alter the results of the test and indeed it does, but fortunately, it is possible to account for the effect of the preload in interpreting the results. The accounting is done by calculating the normalized strength (defined as the strength in the presence of preload ÷ the strength in the absence of preload) as a function of (1) the preloading factor (defined as the preload stress ÷ the strength in the absence of preload) and (2) a SCG parameter, denoted n, that is used in a power-law crack-speed formulation. Figure 2 presents numerical results from this theoretical calculation.

For most glasses and advanced ceramics, the values of n are typically greater than 20. In a typical example, on the basis of the curves in Figure 2, preloading a material of $n = 20$ at 90 percent of its nonpreload strength can be expected to result in an increase of only 0.005 in the normalized strength of the material. At the same time, the 90-percent preload would make it possible to perform the dynamic fatigue test for a given rate in only one-tenth the time of a test at the same rate that starts at zero applied load. In other words, testing time would be greatly reduced, without much effect on the test results.

The theory has been verified by extensive experimentation on a variety of brittle materials, including glasses, a glass-ceramic, and various forms of alumina, silicon nitride, and silicon carbide. This accelerated-testing methodology has been adopted as the basis of two standards of the American Society for Testing and Materials for dynamic fatigue testing of advanced ceramics: C 1368 for ambient temperature and C 1465 for elevated temperatures.
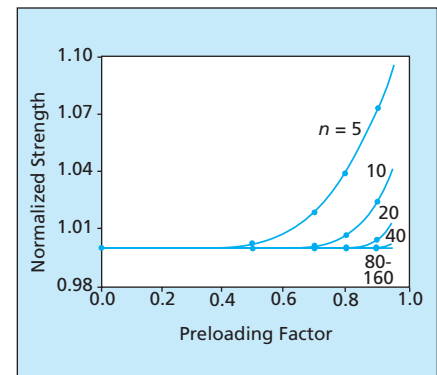
This work was done by John P. Gyekenyesi of **Glenn Research Center** *and Sung R. Choi and Ralph J. Pawlik of Cleveland State University and Ohio Aerospace Institute. Further information is contained in a TSP (see page 1)*

Inquiries concerning rights for the commercial use of this invention should be addressed to NASA Glenn Research Center, Commercial Technology Office, Attn: Steve Fedor, Mail Stop 4-8, 21000 Brookpark Road, Cleveland Ohio 44135. Refer to LEW-17409-1.

⚙ Miniature Blimps for Surveillance and Collection of Samples

These robots could follow complex three-dimensional trajectories through buildings.

NASA's Jet Propulsion Laboratory, Pasadena, California

Miniature blimps are under development as robots for use in exploring the thick, cold, nitrogen atmosphere of Saturn's moon, Titan. Similar blimps can also be used for surveillance and collection of biochemical samples in buildings, caves, subways, and other, similar

1-Meter and 2.3-Meter Radio-Controlled Blimps

Biochemical Collector Filled by Fan Engine

These **Miniature Blimps** are prototypes of radio-controlled, semiautonomous robots for use in preventing and detecting attacks on buildings and their occupants.

structures on Earth. The widely perceived need for means to thwart attacks on buildings and to mitigate the effects of such attacks has prompted consideration of the use of robots. Relative to "rover"-type (wheeled) robots that have been considered for such uses, miniature blimps offer the advantage of ability to move through the air in any direction and, hence, to perform tasks that are difficult or impossible for wheeled robots, including climbing stairs and looking through windows. In addition, miniature blimps are expected to have greater range and to cost less, relative to wheeled robots.

The upper part of the figure depicts two of the blimps, which have lengths of 2.3 and 1 m, and are commercially available as toys or advertising devices. The smaller blimp has a total mass of 200 g, maneuvers by use of fan motors, operates under radio control, and carries a video camera and transmitter. It is equipped with a JPL-fabricated biochemical collector in the form of a small cylinder filled with activated carbon and sandwiched by two open-cell filters. As shown in the lower part of the figure, the biochemical collector is mounted behind a fan motor, so that it automatically becomes filled with gas and/or biochemical dust when the motor is running. To kick up and collect surface dust, the blimp is made to land on its engine cowling and then its fan motors are turned on.

The larger blimp has a total mass of

1.2 kg. It can be filled in 30 seconds from the small bottle shown on the table in the figure. This blimp also operates under radio control and carries a video camera. This blimp has been equipped with an ultralight (170 g) automatic pilot manufactured commercially for radio-controlled small airplanes. This autopilot enables the control system of the blimp to utilize the Global Positioning System in following a trajectory through as many as 60 different waypoints. This autopilot also utilizes ultrasound for precise measurement and control of altitude when the blimp is <5 m above a surface.

For either blimp, the video signal could be utilized in conjunction with target tracking software running on a computer in a remote control station, such that the blimp could automatically approach a target chosen by a remote operator. Either blimp could easily pass through an open door, climb an open stairwell, or rise to look through a window. It could enter an elevator that was remotely operated or that had been manually set to open at a floor under surveillance. It could place small remote surveillance devices and/or relay devices at designated locations, including on ceilings.

This work was done by Jack Jones of Caltech for **NASA's Jet Propulsion Laboratory**. *Further information is contained in a TSP (see page 1)*
NPO-30443

⚙ Hybrid Automotive Engine Using Ethanol-Burning Miller Cycle

This engine would operate with high fuel efficiency and generate little pollution.

Langley Research Center, Hampton, Virginia

A proposed hybrid (internal-combustion/electric) automotive engine system would include as its internal-combustion subsystem, a modified Miller-cycle engine with regenerative air preheating and with autoignition like that of a Diesel engine. The fuel would be ethanol and would be burned lean to ensure com-

plete combustion. Although the proposed engine would have a relatively low power-to-weight ratio compared to most present engines, this would not be the problem encountered if this engine were used in a non-hybrid system since hybrid systems require significantly lower power and thus smaller engines than purely in-

ternal-combustion-engine-driven vehicles. The disadvantage would be offset by the advantages of high fuel efficiency, low emission of nitrogen oxides and particulate pollutants, and the fact that ethanol is a renewable fuel.

The original Miller-cycle engine, named after its inventor, was patented

in the 1940s and is the basis of engines used in some modern automobiles, but is not widely known. In somewhat over-simplified terms, the main difference between a Miller-cycle engine and a common (Otto-cycle) automobile engine is that the Miller-cycle engine has a longer expansion stroke while retaining the shorter compression stroke. This is accomplished by leaving the intake valve open for part of the compression stroke, whereas in the Otto-cycle engine, the intake valve is kept closed during the entire compression stroke. This greater expansion ratio makes it possible to extract more energy from the combustion process without expending more energy for compression. The net result is greater efficiency.

In the proposed engine, the regenerative preheating would be effected by running the intake air through a heat exchanger connected to the engine block. The regenerative preheating would offer two advantages: It would ensure reliable autoignition during operation at low ambient temperature and would help to cool the engine, thereby reducing the remainder of the power needed for cooling and thereby further contributing to efficiency. An electrical-resistance air preheater might be needed to ensure autoignition at startup and during a short warmup period. Because of the autoignition, the engine could operate without either spark plugs or glow plugs.

Ethanol burns relatively cleanly and has been used as a motor fuel since the invention of internal-combustion engines. However, the energy content of ethanol per unit weight of ethanol is less than that of Diesel fuel or gasoline, and ethanol has a higher heat of vaporization. Because the Miller cycle offers an efficiency close to that of the Diesel cycle, burning ethanol in a Miller-cycle engine gives about as much usable output energy per unit volume of fuel as does burning gasoline in a conventional gasoline automotive engine.

Because of the combination of preheating, running lean, and the use of ethyl alcohol, the proposed engine would generate less power per unit volume than does a conventional automotive gasoline engine. Consequently, for a given power level, the main body of the proposed engine would be bulkier.

However, because little or no exhaust cleanup would be needed, the increase in bulk of the engine could be partially offset by the decrease in bulk of the exhaust system. The regenerative preheating also greatly reduces the external engine cooling requirement, and would translate to reduced engine bulk. It may even be possible to accomplish the remaining cooling of the engine by use of air only, eliminating the bulk and power consumption of a water cooling system.

The combination of a Miller-cycle engine with regenerative air preheating, ethyl alcohol fuel, and hybrid operation could result in an automotive engine system that satisfies the need for a low pollution, high efficiency, and simple engine with a totally renewable fuel.

Fabricating Blazed Diffraction Gratings by X-Ray Lithography

Grooves having arbitrarily shaped cross sections can be formed on curved substrates.

NASA's Jet Propulsion Laboratory, Pasadena, California

Gray-scale x-ray lithography is undergoing development as a technique for fabricating blazed diffraction gratings. As such, gray-scale x-ray lithography now complements such other grating-fabrication techniques as mechanical ruling, holography, ion etching, laser ablation, laser writing, and electron-beam lithography. Each of these techniques offers advantages and disadvantages for implementing specific grating designs; no single one of these techniques can satisfy the design requirements for all applications.

Gray-scale x-ray lithography is expected to be advantageous for making gratings on steeper substrates than those that can be made by electron-beam lithography. This technique is not limited to sawtooth groove profiles and flat substrates: various groove profiles can be generated on arbitrarily shaped (including highly curved) substrates with the same ease as sawtooth profiles can be generated on flat substrates. Moreover, the gratings fabricated by this technique can be made free of ghosts (spurious diffraction components attributable to small spurious periodicities in the locations of grooves).
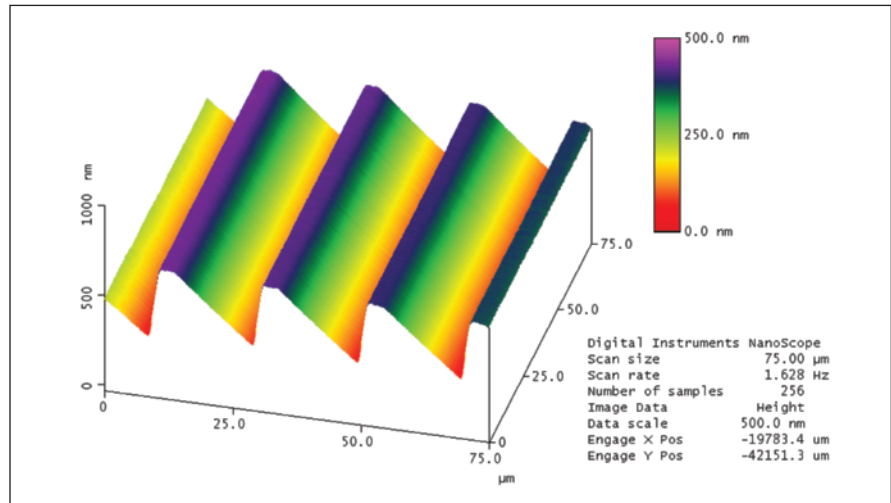
The first step in gray-scale x-ray lithog-

Figure 2: **Atomic Force Microscope Scan** of grooves is generated through this technique. The period is 20 μm. The peak efficiency was measured to be 82 percent.

raphy is to conformally coat a substrate with a suitable photoresist. An x-ray mask (see Figure 1) is generated, placed between the substrate and a source of collimated x-rays, and scanned over the substrate so as to create a spatial modulation in the exposure of the photoresist. Development of the exposed photoresist results in a surface corrugation that corresponds to the spatial modulation and that defines the grating surface.

The grating pattern is generated by scanning an appropriately shaped x-ray area mask along the substrate. The mask example of Figure 1 would generate a blazed grating profile when scanned in the perpendicular direction at constant speed, assuming the photoresist responds linearly to incident radiation. If the resist response is nonlinear, then the mask shape can be modified to account for the nonlinearity and produce a desired groove profile. An example of grating grooves generated by

this technique is shown in Figure 2. A maximum relative efficiency of 88 percent has been demonstrated.

Figure 1. **Sample X-Ray Mask** is shown with a period of 9 μm and gold thickness of 5 μm.

Freeze-Tolerant Condensers

Two designs offer similar advantages.

Lyndon B. Johnson Space Center, Houston, Texas

Two condensers designed for use in dissipating heat carried by working fluids feature two-phase, self-adjusting configurations such that their working lengths automatically vary to suit their input power levels and/or heat-sink temperatures. A key advantage of these condensers is that they can function even if the temperatures of their heat sinks fall below the freezing temperatures of their working fluids and the fluids freeze. The condensers can even be restarted from the frozen condition.

The top part of the figure depicts the layout of the first condenser. A two-phase (liquid and vapor) condenser/vapor tube is thermally connected to a heat sink — typically, a radiatively or convectively cooled metal panel. A single-phase (liquid) condensate-return tube (return artery) is also thermally connected to the heat sink. At intervals along their lengths, the condenser/vapor tube and the return artery are interconnected through porous plugs. This condenser configuration affords tolerance of freezing, variable effective thermal conductance (such that the return temperature remains

nearly constant, independently of the ultimate sink temperature), and overall pressure drop smaller than it would be without the porous interconnections. An additional benefit of this configuration is that the condenser can be made to recover from the completely frozen condition either without using heaters, or else with the help of heaters much smaller than would otherwise be needed.

The second condenser affords the same advantages and is based on a similar principle, but it has a different configuration that affords improved flow of working fluid, simplified construction, reduced weight, and faster recovery from a frozen condition. The major difference between the second and first condensers are the following:

• In the first condenser, the condenser/vapor tube and the return artery lie alongside each other. In the second condenser, the return artery is narrower than it is in the first condenser and lies within the vapor/condenser tube, as shown in the lower part of the figure.

• In the second condenser, there are no

discrete porous interconnections. Instead, the wall of the return artery is porous along the entire common length of the return artery and condenser/vapor tubes. The porous return artery can be fabricated by any of a variety of techniques, including micromachining of a narrow tube, rolling metal screens, or extrusion of initially porous tubing material. The pores must be narrow enough that the capillary pressure exceeds the total pressure drop from the vapor inlet to the return-artery outlet, so that vapor does not blow through the pores to the return artery.

• A small, possibly optional, electrical "starter" heater is located at the condenser inlet.

The second condenser weighs less than the first condenser does because the return artery in the second condenser is (1) narrower than that of the first condenser and (2) can have a very thin wall without risk of rupture because, unlike in the first condenser, it is not a significant pressure boundary. In comparison with the first condenser, the second condenser is both simpler to construct and more reliable because, in the absence of the discrete porous interconnections and the associated fittings, fewer welds are needed. Finally, the continuous distribution of porous interconnection in second condenser (in contradistinction to the discrete porous interconnections of the first condenser) make it possible for the second condenser to be thawed more rapidly.
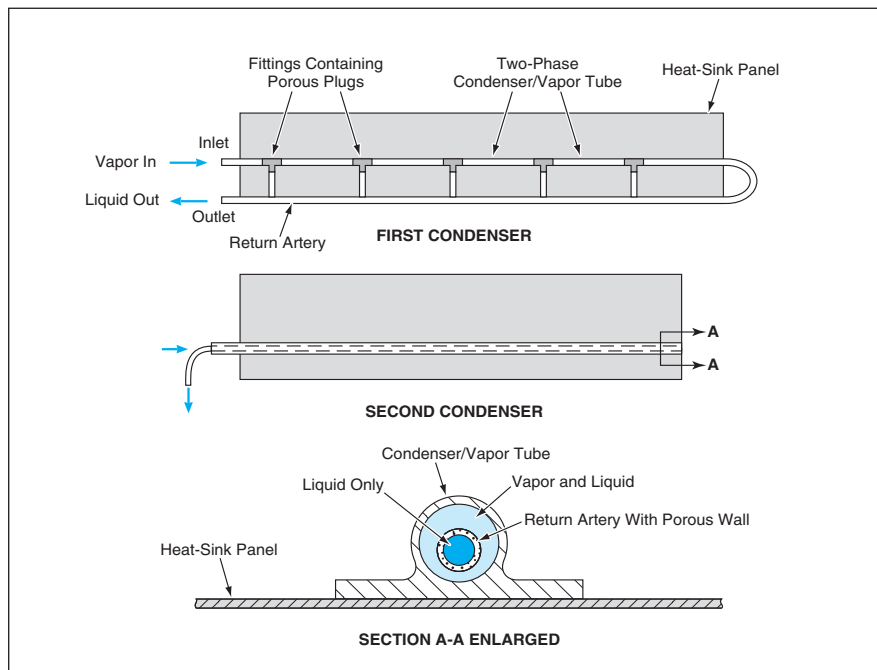
These **Freeze-Tolerant Condensers** differ in their flow geometries and the distributions of their porous interconnections.

The StarLight Space Interferometer

NASA's Jet Propulsion Laboratory, Pasadena, California

Two papers describe the StarLight space interferometer — a Michelson interferometer that would be implemented by two spacecraft flying in formation. The StarLight formation flying interferometer project has been testing and demonstrating engineering concepts for a new generation of space interferometers that would be employed in a search for extrasolar planets and in astrophysical investigations. As described in the papers, the original StarLight concept called for three space-craft, and the main innovation embodied is a modification that makes it possible to reduce complexity by eliminating the third spacecraft. The main features of the modification are (1) introduction of an optical delay line on one spacecraft and (2) controlling the flying formation such that the two spacecraft are located at two points along a specified parabola so as to define the required baseline of specified length (which could be varied up to 125 m) perpendicular to the axis of the parabola. One of the papers presents a detailed description of the optical layout and discusses computational modeling of the performance; the other paper presents an overview of the requirements for operation and design, the overall architecture, and subsystems.

This work was done by William Folkner, Michael Shao, and Peter Gorham of Caltech for **NASA's Jet Propulsion Laboratory**. *Further information is contained in a TSP (see page 1)*
NPO-30726

Champagne Heat Pump

**Relatively safe and environmentally benign working fluids can be used.**

NASA's Jet Propulsion Laboratory, Pasadena, California

The term "champagne heat pump" denotes a developmental heat pump that exploits a cycle of absorption and desorption of carbon dioxide in an alcohol or other organic liquid. Whereas most heat pumps in common use in the United States are energized by mechanical compression, the champagne heat pump is energized by heating.

The concept of heat pumps based on other absorption cycles energized by heat has been understood for years, but some of these heat pumps are outlawed in many areas because of the potential hazards posed by leakage of working fluids. For example, in the case of the water/ammonia cycle, there are potential hazards of toxicity and flammability.

The organic-liquid/carbon dioxide absorption/desorption cycle of the champagne heat pump is similar to the water/ammonia cycle, but carbon dioxide is nontoxic and environmentally benign, and one can choose an alcohol or other organic liquid that is also relatively nontoxic and environmentally benign. Two candidate nonalcohol organic liquids are isobutyl acetate and amyl acetate. Although alcohols and many other organic liquids are flammable, they present little or no flammability hazard in the champagne heat pump because only the nonflammable carbon dioxide component of the refrigerant mixture is circulated to the evaporator and condenser heat exchangers, which are the only components of the heat pump in direct contact with air in habitable spaces.

The champagne heat pump (see figure) includes a generator — essentially a heated pressure vessel — wherein a solution of carbon dioxide in the absorbent liquid is heated to generate pressurized carbon dioxide. In a typical application, the solution is heated to a temperature of 250 °F (121 °C), causing the carbon dioxide to be desorbed at a pressure of about 1.4 kpsi (9.7 MPa). The carbon dioxide is precooled, typically to about 100 °F (38 °C) while at this high pressure, then expanded to a pressure of about 560 psi (3.9 MPa); this expansion provides cooling to about 40 °F (4 °C). The carbon dioxide then passes back through a heat exchanger to an absorber, which is another pressure vessel wherein the carbon diox-
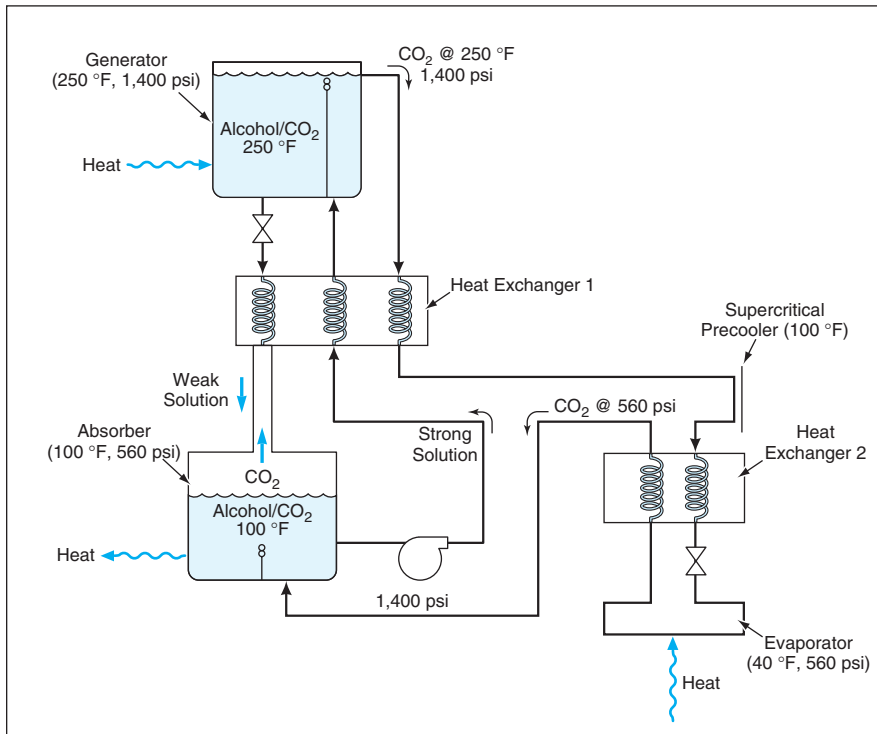
Carbon Dioxide Is Absorbed and Desorbed in a thermodynamic cycle similar to that of a water/ammonia heat pump. The champagne heat pump is so named because the desorption part of its operating cycle is reminiscent of carbon dioxide effervescing out of alcohol-containing champagne.

ide goes back into solution, releasing heat. A pump circulates the solution between the generator and absorber.

Carbon dioxide can be an excellent refrigerant fluid for automobiles because its critical temperature is only about 88 °F (31 °C). Therefore, precooling prior to expansion can take place over a relatively wide supercritical temperature range; in contrast, the common refrigerant 134a must be condensed at one specific temperature for a given pressure.

A research group in Norway has produced mechanically actuated carbon dioxide vapor-compression air conditioners for automobiles and has shown those air conditioners to be more efficient and potentially lighter than are comparable air conditioners based on a chlorofluorocarbon refrigerant fluid. The champagne heat pump goes beyond the Norwegian research by replacing mechanical actuation with heat actuation. Potential applications (other than automotive air conditioning) for the champagne heat pump include home and industrial heating and cooling.

This work was done by Jack A. Jones of Caltech for **NASA's Jet Propulsion Laboratory**. *Further information is contained in a TSP (see page 1)*

This invention is owned by NASA, and a patent application has been filed. Inquiries concerning nonexclusive or exclusive license for its commercial development should be addressed to the Patent Counsel, NASA Management Office–JPL; (818) 354-7770. Refer to NPO-19855.

Controllable Sonar Lenses and Prisms Based on ERFs
Compact devices without moving parts would focus and steer acoustic beams.
NASA's Jet Propulsion Laboratory, Pasadena, California

Sonar-beam-steering devices of the proposed type would contain no moving parts and would be considerably smaller and less power-hungry, relative to conventional multiple-beam sonar arrays. The proposed devices are under consideration for installation on future small autonomous underwater vehicles because the sizes and power demands of conventional multiple-beam arrays are excessive, and motors used in single-beam mechanically scanned systems are also not reliable.

The proposed devices would include a variety of electrically controllable acoustic prisms, lenses, and prism/lens combinations – both simple and compound. These devices would contain electrorheological fluids (ERFs) between electrodes. An ERF typically consists of dielectric particles floating in a dielectric fluid. When an electric field is applied to the fluid, the particles become grouped into fibrils aligned in rows, with a consequent increase in the viscosity of the fluid and a corresponding increase in the speed of sound in the fluid. The change in the speed of sound increases with an increase in the applied electric field. By thus varying the speed of sound, one varies the acoustic index of refraction, analogously to varying the index of refraction of an optical lens or prism. In the proposed acoustic devices, this effect would be exploited to control the angles of refraction of acoustic beams, thereby steering the beams and, in the case of lenses, controlling focal lengths.

Figure 1 schematically illustrates a sonar assembly according to the proposal. A planar array of acoustic transmitting/receiving transducers would both send out acoustic signals to irradiate targets and, in the acoustic analog of a retina, sense the spatial pattern of return acoustic signals. The transmitted and return signals would be collimated and focused, respectively, by use of two acoustic lenses. The front acoustic lens would be designed to contain an ERF in multiple compartments separated by electrodes, rather than one compartment between a single pair of outer electrodes, in
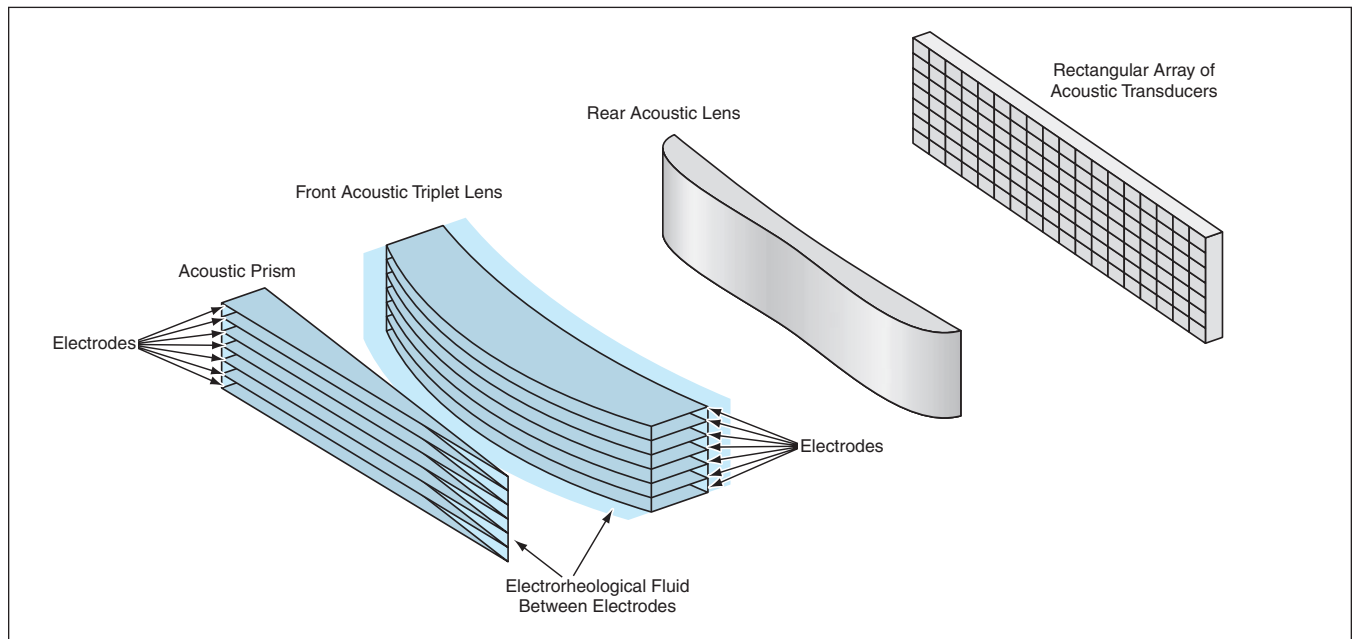

Figure 1. **Electric Fields Would Be Applied** to electrorheological fluids between electrodes to vary the indices of refraction of the acoustic prism and lens, thereby varying the beam direction and focal length, respectively.

order to reduce the magnitudes of the potentials needed to be applied to the electrodes to vary the focal length of the lens through the required range. A prism in
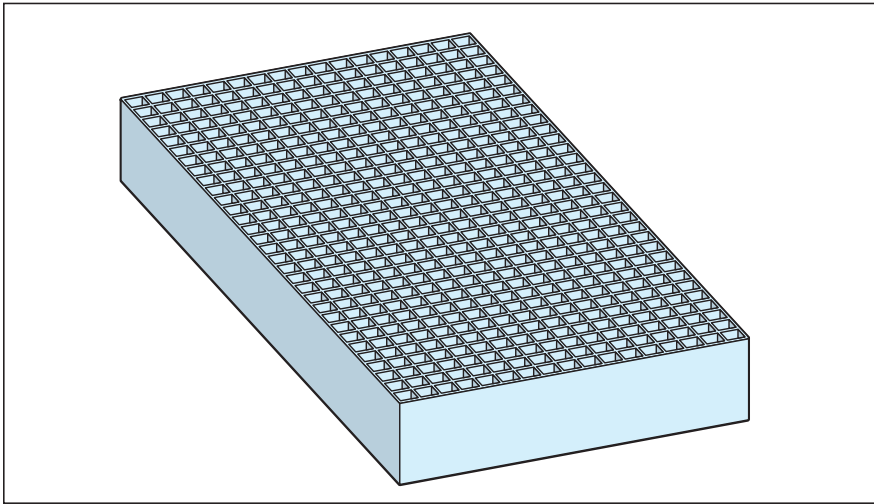

Figure 2. **Cells in a Rectangular Array** would be filled with an electrorheological fluid. Electrodes on the walls between the cells would make it possible to apply electric fields to individual cells along the row and column directions.

front of the front lens would also be constructed in layers, for the same reason. The index of refraction of the prism and, hence, the angle of refraction of the beam, would

be varied by modulating the potentials applied to the prism electrodes in order to steer the outgoing and incoming acoustic beams.

The concept of ERF-filled compartments separated by electrodes could be generalized and modified to that of a multicellular device comprising a rectangular array of ERF-filled cells (see Figure 2). Electrodes would be affixed to both the row and the column walls between cells, so that an electric field of controlled magnitude and direction could be applied to the ERF within each cell. Lens shape (convex, concave, etc.) can be varied by selectively activating individual cells.

Measuring Gravitation Using Polarization Spectroscopy
Numbers of cold atoms could also be measured.

NASA's Jet Propulsion Laboratory, Pasadena, California

A proposed method of measuring gravitational acceleration would involve the application of polarization spectroscopy to an ultracold, vertically moving cloud of atoms (an atomic fountain). A related proposed method involving measurements of absorption of light pulses like those used in conventional atomic interferometry would yield an estimate of the number of atoms participating in the interferometric interaction.

The basis of the first-mentioned proposed method is that the rotation of polarization of light is affected by the acceleration of atoms along the path of propagation of the light. The rotation of polarization is associated with a phase shift: When an atom moving in a laboratory reference interacts with an electromagnetic wave, the energy levels of the atom are Doppler-shifted, relative to where they would be if the atom were stationary. The Doppler shift gives rise to changes in the detuning of the light from the corresponding atomic transitions. This detuning, in turn, causes the electromagnetic wave to undergo a phase shift that can be measured by conventional means. One would infer the gravitational acceleration and/or the gradient of the

gravitational acceleration from the phase measurements.

The figure depicts the optical layout of a version of an apparatus that would be used in the proposed method to measure the gravitational acceleration. (A slightly different version would be used to measure a gradient in the gravitational acceleration.) Also shown is a diagram of the relevant energy levels of atoms of an element suitable for use in these methods: The element must be one that has a Λ-shaped energy-level scheme as depicted here. A linearly polarized laser beam would impinge on a first polarizing beam splitter (PBS1), which would divide the beam into two beams of equal power. By use of quarter-wave plates, the two beams would be given opposite circular polarizations. One of the two beams would be steered to propagate upward, the other to propagate downward along a vertical tube containing an ultracold cloud of the atoms in question.
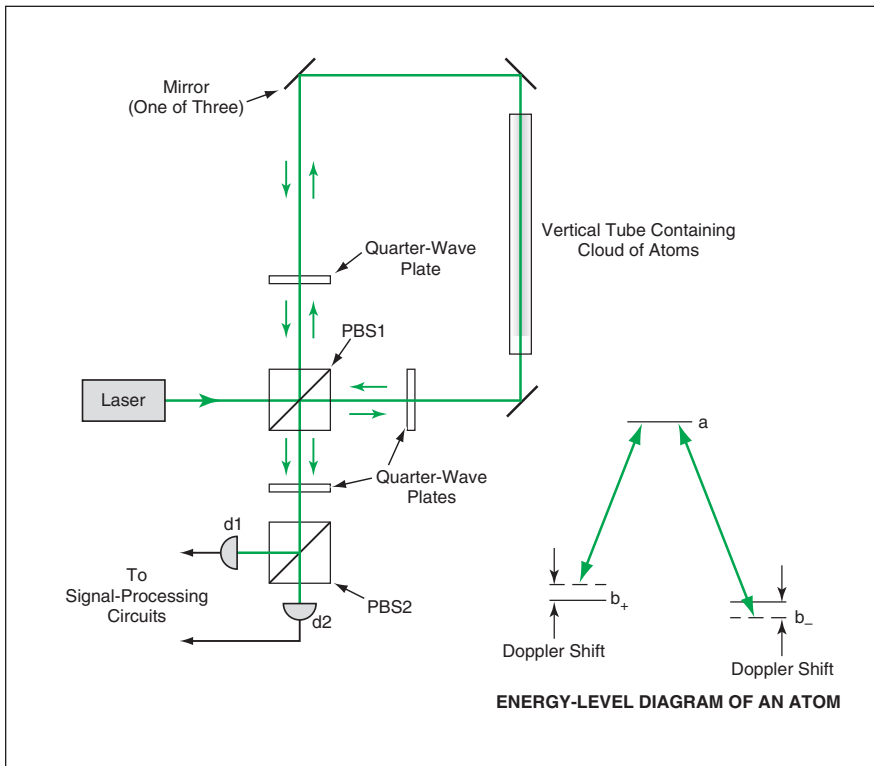
After propagating through the cloud, the beams would be converted back to linear polarizations by the same quarter-wave plates, then recombined in PBS1 to produce an output beam, which would

be steered through a quarter-wave plate oriented at 45° with respect to the original linear polarization. This quarter-wave plate would transform the beam into a linearly polarized beam, the polarization direction of which would differ from that of the original laser light by an angle, ϕ, that would depend on the velocity of the atoms. A second polarizing beam splitter (PBS2), also oriented at 45° with respect to the original polarization, would split the beam into two parts that would go to two photodiodes (d1 and d2). The output currents of the two photodiodes would be proportional to

$$(1/2)[P_+ + P_- \pm 2(P_+P_-)^{1/2}\sin(2\phi)],$$

where P_+ and P_- denote the powers of the two opposite circularly polarized beams. The sum of the two photocurrents would be proportional to the total output power, while the difference between them would give information on the polarization-rotation angle, ϕ.

A lengthy mathematical derivation that must be omitted here for the sake of brevity leads to an equation for dependence of ϕ on a number of variables that include time (t) and the gravitational acceleration (g). The equation could be used to infer g from the mea-

Mirror
(One of Three)

Quarter-Wave
Plate

PBS1

Laser

Vertical Tube Containing
Cloud of Atoms

Quarter-Wave
Plates

d1

To
Signal-Processing
Circuits

d2

PBS2

a

b_+

Doppler Shift

b_-

Doppler Shift

ENERGY-LEVEL DIAGRAM OF AN ATOM

An **Ultracold Cloud of Atoms** having a Λ-shaped energy-level scheme, contained in a vertical tube, would be probed by means of time-dependent polarization spectroscopy. The apparatus would yield phase-shift measurements from which gravitational acceleration could be inferred.

surements. A further derivation shows that the signal-to-noise ratio would be maximized by filtering the photodetector outputs via an appropriate time-dependent function and by choosing an optimum number of photons, which turns out to equal the number of atoms interacting with the light.

In the second-mentioned proposed method (the one for estimating the number of atoms participating in interferometric interactions), one would exploit the connection between the number of photons and the atomic state-population in a Raman configuration. As in the method described above, the atoms to be probed must have a Λ-shaped energy-level scheme. One would utilize light pulses that are already used to prepare the atomic cloud in a particular quantum state in conventional atomic interferometer schemes. Yet another mathematical derivation shows that the difference between the numbers of photons of two counter-propagating electromagnetic fields used to generate the pulses is related to the number of participating atoms. This method of atomic-population measurement may offer sensitivity greater than is offered by any prior method. This method would increase the sensitivities afforded by pre-existing atomic-interferometry schemes, without need to change those schemes significantly. Moreover, the measurements of the light pulses may also yield rough estimates of the expected interferometric signals.

Information Sciences

Serial-Turbo-Trellis-Coded Modulation With Rate-1 Inner Code
Coders and decoders for bandwidth- and power-limited systems could be less complex.

NASA's Jet Propulsion Laboratory, Pasadena, California

Serially concatenated turbo codes have been proposed to satisfy requirements for low bit- and word-error rates and for low (in comparison with related previous codes) complexity of coding and decoding algorithms and thus low complexity of coding and decoding circuitry. These codes are applicable to such high-level modulations as octonary phase-shift keying (8PSK) and 16-state quadrature amplitude modulation (16QAM); the signal product obtained by applying one of these codes to one of these modulations is denoted, generally, as "serially concatenated trellis-coded modulation" ("SCTCM"). These codes could be particularly beneficial for communication systems that must be designed and operated subject to limitations on bandwidth and power.

Some background information is prerequisite to a meaningful summary of this development. Trellis-coded modulation (TCM) is now a well-established technique in digital communications. A turbo code combines binary component codes (which typically include trellis codes) with interleaving. A turbo code of the type that has been studied prior to this development is composed of parallel concatenated convolutional codes (PCCCs) implemented by two or more constituent systematic encoders joined through one or more interleavers. The input information bits feed the first encoder and, after having been scrambled by the interleaver, enter the second encoder. A code word of a parallel concatenated code consists of the input bits to the first encoder followed by the parity check bits of both encoders. The suboptimal iterative decoding structure for such a code is modular, and consists of a set of concatenated decoding modules — one for each constituent code — connected through an interleaver identical to the one in the encoder side. Each decoder performs weighted soft decoding of the input sequence. PCCCs yield very large coding gains at the cost of a reduction in the data rate and/or an increase in bandwidth.

As its full name suggests, SCTCM merges serially concatenated convolu-

tional codes (SCCCs) with TCM. SCTCM is believed to offer the potential to achieve low bit-error rates ($\leq 10^{-9}$), in part because the error floors of SCCCs are lower than those of PCCCs.

It is important to note that the proposed serial concatenated coding scheme differs from "classical" concatenated coding schemes. In a classical scheme, the role of the interleaver between two encoders is merely to break up bursts of errors produced by the inner decoder, and no attempt is made to consider the combination of the two encoders and the interleaver as a single entity. In SCTCM, on the other hand, one seeks to optimize the whole serial structure.

No attempt at such optimization was made in the past, in part because optimizing an overall code with large deterministic interleavers is prohibitively complex. However, by introducing the concept of a uniform interleaver, it is possible to draw some criteria to optimize the component codes for the construction of powerful serially concatenated codes with large block size. Another reason optimization of overall codes was not attempted is that optimum decoding of complex codes is practically impossible; only the use of suboptimum iterative decoding techniques makes it possible to decode such complex codes. The decoder in an SCTCM system would utilize an adapted version of iterative decoding used in PCCC schemes.

The upper part of the figure is a block diagram of an encoder in an SCTCM system that yields a bit-rate-to-bandwidth ratio of b (bits/second)/Hertz when

ideal Nyquist pulse shaping is used. The outer encoder implements a rate-$[2b/(2b+1)]$ binary convolutional code (or a short block code) with maximum free Hamming distance (or minimum distance). The interleaver (π) permutes the output of the outer encoder. The interleaved data enter the inner encoder, which implements a rate-$[(2b+1)/(2b+2)]$ recursive convolutional code. The $2b+2$ output bits are then mapped to two symbols, each belonging to a 2^{b+1}-point two-dimensional constellation. This results in four-dimensional modulation. In this way, $2b$ information bits are used for every two modulation symbol intervals; in other words, there are b information bits per modulation symbol. The inner code and the mapping are jointly optimized on the basis of maximizing the effective free Euclidean distance of the inner TCM.

Unfortunately, the decoder associated with such an encoder would be unacceptably complex and thus unsuitable for high-speed operation. This is because the number of transitions per state for the inner TCM is 2^{2b+1} and so the number of edges in the trellis section of the decoder would have to equal to 2^{2b+1} × the number of states.

The lower part of the figure is a block diagram of an SCTCM encoder for an M-point two-dimensional constellation that would enable the use of a decoder of lower complexity. This encoder yields a bit-rate-to-bandwidth ratio of $bm/(b+1)$ (bits/second)/Hertz [where $m \equiv \log_2 M$ and M is the number of points in a two-dimensional signal constellation] when ideal Nyquist pulse shaping is used. The outer encoder implements a rate-
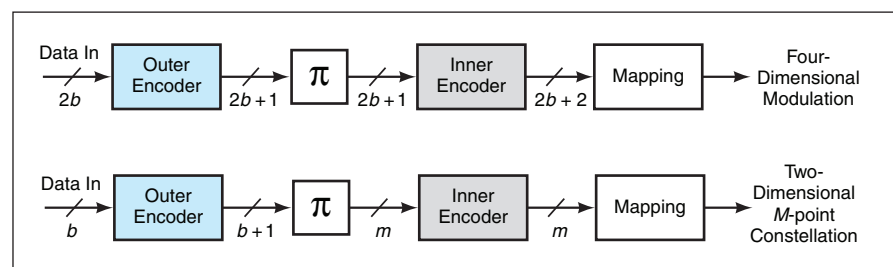
These **Encoders** implement two SCTCM schemes. Both encoders generate powerful codes, but the one of the lower diagram enables the use of a simpler decoder.

$[b/(b+1)]$ binary convolutional code (or a short block code) with maximum free Hamming distance (or minimum distance). The interleaver (π) permutes the output of the outer encoder. The interleaved data enter the inner encoder, which implements a rate-(m/m) [rate-1] recursive convolutional code. The m output bits are then mapped to one symbol that belongs to a 2^m-level modulation. Because the inner code does not have redundancy, it is useless by itself; however, the combination of the inner and outer codes with the interleaver results in very powerful code. For MQAM where $M = N^2$, further reduction in complexity is possible. This can be done by assigning the $m = \log_2 N$ output bits of the inner encoder alternately to the inphase and quadrature components of N^2QAM modulation. In this case, the bit-rate-to-bandwidth ratio will be

$$2bm/(b+1).$$

The advantage of this generic design can be made more apparent by citing an example of $b = 3$ for 16QAM, for which $m = 2$. In this example, the number of transitions per state of the inner TCM is only 4, which is only $1/32$ of the corresponding number for the previous case.

This work was done by Dariush Divsalar, Sam Dolinar, and Fabrizio Pollara of Caltech

Enhanced Software for Scheduling Space-Shuttle Processing
Prototype software has been upgraded.

John F. Kennedy Space Center, Florida

The Ground Processing Scheduling System (GPSS) computer program is used to develop streamlined schedules for the inspection, repair, and refurbishment of space shuttles at Kennedy Space Center. A scheduling computer program is needed because space-shuttle processing is complex and it is frequently necessary to modify schedules to accommodate unanticipated events, unavailability of specialized personnel, unexpected delays, and the need to repair newly discovered defects. GPSS implements constraint-based scheduling algorithms and provides an interactive scheduling software environment. In response to inputs, GPSS can respond with schedules that are optimized in the sense that they contain minimal violations of constraints while supporting the most effective and efficient utilization of space-shuttle ground processing resources.

The present version of GPSS is a product of re-engineering of a prototype version. While the prototype version proved to be valuable and versatile as a scheduling software tool during the first five years, it was characterized by design and algorithmic deficiencies that affected schedule revisions, query capability, task movement, report capability, and overall interface complexity. In addition, the lack of documentation gave rise to difficulties in maintenance and limited both enhanceability and portability.

The goal of the GPSS re-engineering project was to upgrade the prototype into a flexible system that supports multiple-flow, multiple-site scheduling and that retains the strengths of the prototype while incorporating improvements in maintainability, enhanceability, and portability. The major enhancements were the following:

• The implementation of container objects (e.g., lists and maps) was made more efficient by use of the C++ Standard Template Library (STL).

• Improvements in the management of schedule network objects were made. An embedded schedule-data configuration-management subsystem, similar to systems used for software configuration management, was built. This subsystem accommodates multiple versions and revisions of each schedule, including direct descendants and branches. It also implements a concept of user sessions that enables each user to maintain multiple current instances of the same schedule and full schedule data files with sizes of the order of 1MB.

• Improvements in calendar operations were made. The original implementation required the full, time-series expansion of all calendars, giving rise to a large memory overhead. Furthermore, some calendar features (e.g., holidays), were "hard-coded." In the re-engineering, calendar memory requirements were reduced by providing for all calendar calculations to be performed in real time and by removing all hard-coded elements.

• Re-engineering of a robust query subsystem was perhaps the most challenging aspect of the project. The prototype utilized a Prolog-like query language that was scanned, parsed, and executed in a C program. The query code was problematic and difficult to understand. The re-engineering involved the building of a real (but similar) query language, utilizing the FLEX language and the Bison program to define a scanner and parser that includes all elements of logical inference (for example, AND, OR, and NOT) as well as full capability for building and incorporating user-customizable queries.

• An improved report architecture was developed. The prototype featured a significant number of hard-coded user options, and too little care was taken initially to develop a consistent but flexible report architecture. The re-engineering of the affected software components involved design around a new report class that contains attributes that describe the class of objects (e.g., tasks) represented in a report, the presentation style (e.g., Gantt chart or tabulation), and the time frame of the report. All report definitions are saved in files that the user can edit to customize reports.

• Several improvements in algorithms were made to solve backward-movement problems, provide a more robust implementation of achievers, and improve memory management through the use of smart pointers and "lazy load" of persistent data. Also included

is an updated implementation of an object-oriented callback system to the Motif widget set.

The benefits of the re-engineered version of GPSS hinge on the object-oriented approach. The use of STL and the improvements in schedule and query operations are incorporated in C++ libraries that may prove useful on succeeding projects. The rewriting of software in C++ in-

creases portability. For the users, every effort was made in the re-engineering to maximize flexibility and improve upon the intuitive nature of the interface without sacrificing any of the capabilities that made the prototype successful.

Bayesian-Augmented Identification of Stars in a Narrow View
An adaptive threshold guides acceptance or rejection of a tentative identification.

NASA's Jet Propulsion Laboratory, Pasadena, California

An algorithm for the identification of stars from a charge-coupled-device (CCD) image of a star field has been extended for use with narrower field-of-view images. Previously, the algorithm had been shown to be effective at a field of view of 8°. This work augments the earlier algorithm using Bayesian decision theory. The new algorithm is shown to be capable of effective star identification down to a field of view of 2°. The algorithm was developed for use in estimating the attitude of a spacecraft and could be used on Earth to help in the identification of stars and other celestial objects for astronomical observations.

The present algorithm is one of several that seek matches between (1) imaged star fields and (2) portions of the sky, with angular dimensions equal to those of the imaged star fields, in a catalog of stars in a known reference frame. Previously developed star-identification algorithms are not suitable for fields of

view only 2° wide. The present algorithm is based partly on one such prior algorithm, called the "grid algorithm," that has shown promise for identifying stars in fields of view 8° wide. To make it possible to identify stars in fields of view down to 2° with acceptably low probabilities of error, the grid algorithm has been extended by incorporating Bayesian decision theory.

For the special purpose of the grid algorithm, the term "pattern" denotes a grid representation of the relative positions of stars in a field of view. Each star is deemed to be located within one of the cells of a square grid that spans either the field of view of the CCD image or a candidate star-catalog field of the same angular dimensions. The portion of the grid algorithm that generates a pattern comprises the following steps (see figure):

1. Choose a star from the CCD image or the applicable field of view in the star
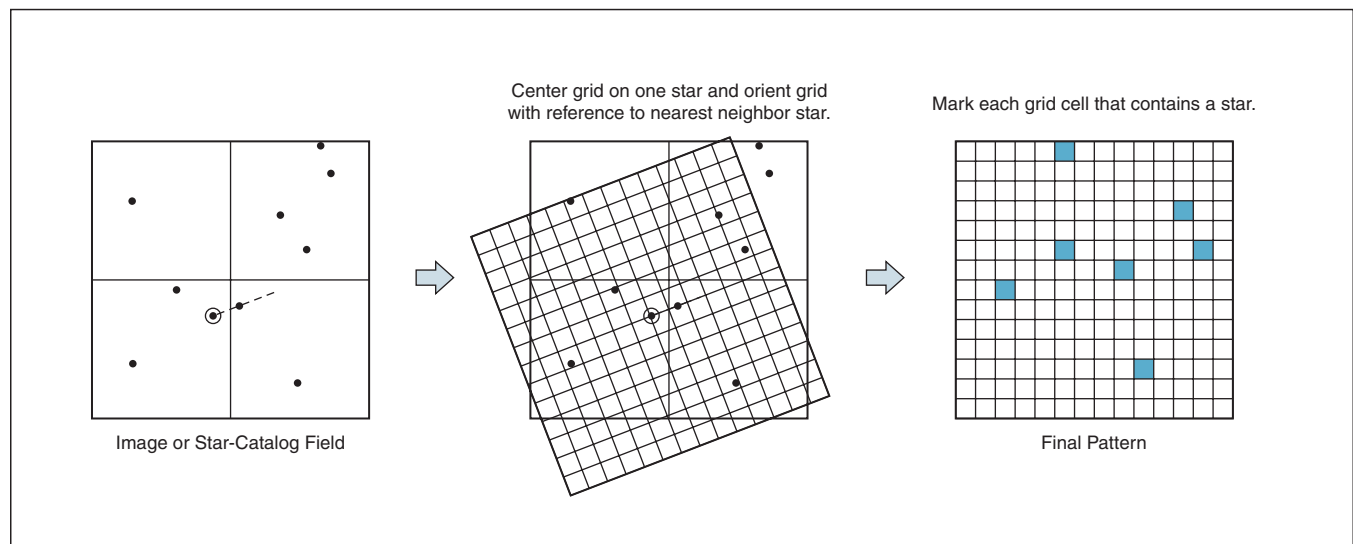
catalog to be the center star.
2. Decide which star is the neighbor star. The neighbor star is deemed to be the star nearest to the center star outside a buffer radius of *br* pixels. The value of *br* is chosen on the basis of experience.
3. Center a grid of *g* rows and *g* columns on the center star, and orient the grid such that a horizontal vector from the center to the right edge passes through the neighbor star. Like *br*, the value of *g* is chosen on the basis of experience.
4. Derive a pattern, a g^2-element bit vector

$$V[0 \ldots g^2 - 1]$$

such that if grid cell (i,j) contains a star, then

$$V[jg + i] = 1$$

The vector element corresponding to any grid cell which does not contain a star is given the value 0. The dot product

Center grid on one star and orient grid with reference to nearest neighbor star.

Mark each grid cell that contains a star.

Image or Star-Catalog Field

Final Pattern

A **Grid Pattern** is created from either a CCD image of stars or star-catalog data for a field of view of the same angular dimensions as those of the CCD image.

is used to measure how well two patterns V and W match:

$$m = \sum_i V_i W_i.$$

The identification problem then becomes that of finding a catalog pattern that matches the CCD-image pattern. In a typical case, several sources of noise make it impossible to find a perfect match, making it necessary to use a quantitative criterion to decide whether one should accept an imperfect match. One such source is location noise: a star can appear in a grid cell different from that in the catalog. Another such source is magnitude (brightness) noise that affects stars at and near the limit of detectability by the CCD: some stars considered too dim to be included in the catalog could appear in the CCD image, and some stars included in the catalog could be excluded from the CCD image. Still another source of noise is that in the process of producing a pattern centered on a star which is near the edge of the CCD image, some of the grid cells may not be covered by the image. These cells will not contain stars. However, these cells in the corresponding catalog pattern may contain stars.

In the original grid algorithm, the count of stars (m) which match between a CCD image pattern and some catalog pattern is compared against a fixed threshold to determine if the match is good enough to identify the center star. In the augmented algorithm, this fixed threshold has been replaced by an adaptive, probabilistic threshold which takes into account (a) the number of stars in each of the two patterns and (b) the proportion of grid cells in the image pattern lost due to proximity with the edge of the image.

The augmented algorithm has been tested in computer simulations, using a catalog of 934,487 stars brighter than 11th magnitude, along with a variety of different assumed noise conditions. For a $2° \times 2°$ field of view projected onto a CCD of $1,024 \times 1,024$ pixels, a standard deviation of 0.5 pixel in the position of each star as imaged on the CCD, and a brightness deviation of 0.8 stellar magnitude, the algorithm yielded correct identifications in 96 percent of the test examples and false positives in only 0.3 percent of the examples.

Books & Reports

☢ Spacecraft Orbits for Earth/Mars-Lander Radio Relay

A report discusses a network of spacecraft, in orbit around Mars, used to relay radio communications between Earth stations and mobile exploratory robots (rovers) as well as stationary scientific instruments that have been landed on the Mars surface. The relay spacecraft include two already in orbit plus several others planned to arrive at Mars in the years 2004 through 2008. A major portion of the report is devoted to the orbit of the G. Macroni Orbiter, which is in the midst of an iterative design process and is intended to be the first Mars orbiter designed primarily for radio relay. Candidate orbits are analyzed with a view toward choosing one that maximizes the amount of time available for communication with surface units, taking account of visibility as a function of position, the limit on communication distance at low power, and the fact that surface units can transmit more easily when they are in sunlight. Two promising new orbits for Mars relay satellites are identified: a 1/2-sol apoapsis-at-constant-time-of-day equatorial orbit and a 1/4-sol apoapsis-at-constant-time-of-day, critical-inclination orbit.
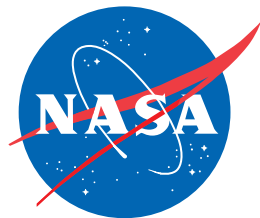
This work was done by Gary Noreen, Roger Diehl, and Joseph Neelon of Caltech for **NASA's Jet Propulsion Laboratory**. *Further information is contained in a TSP (see page 1)*
NPO-30639

☢ Self-Inflatable/Self-Rigidizable Reflectarray Antenna

A report describes recent progress in a continuing effort to develop large reflectarray antennas to be deployed in space. Major underlying concepts were reported in two prior *NASA Tech Briefs* articles: "Inflatable Reflectarray Antennas" (NPO-20433), Vol. 23, No. 10 (October 1999), page 50 and "Tape-Spring Reinforcements for Inflatable Structural Tubes" (NPO-20615), Vol. 24, No. 7 (July 2000), page 58. To recapitulate: An antenna as proposed would include a reflectarray membrane stretched flat on a frame of multiple tubular booms that would be deployed by inflation. The instant report discusses design concepts and relevant basic mechanical principles. Among the concepts are alternative configurations of booms for holding the reflectarray membrane and its radio-frequency feed horn and the use of catenaries and constant-force springs to stretch the reflectarray membrane on the frame at the required tension. Some emphasis is placed on the need to keep the deployed frame rigid without depending on maintenance of inflation in the presence of impinging micrometeors that could cause leaks: for this purpose, the booms could be made as spring-tape-reinforced aluminum laminate tubes like those described in the second-mentioned prior article.

This work was done by Houfei Fang, Michael Lou, and John Huang of Caltech for **NASA's Jet Propulsion Laboratory**. *Further information is contained in a TSP (see page 1).*
NPO-30662

National Aeronautics and
Space Administration